Article

Neuron

Neuronal Architecture of a Visual Center that Processes Optic Flow

Graphical Abstract

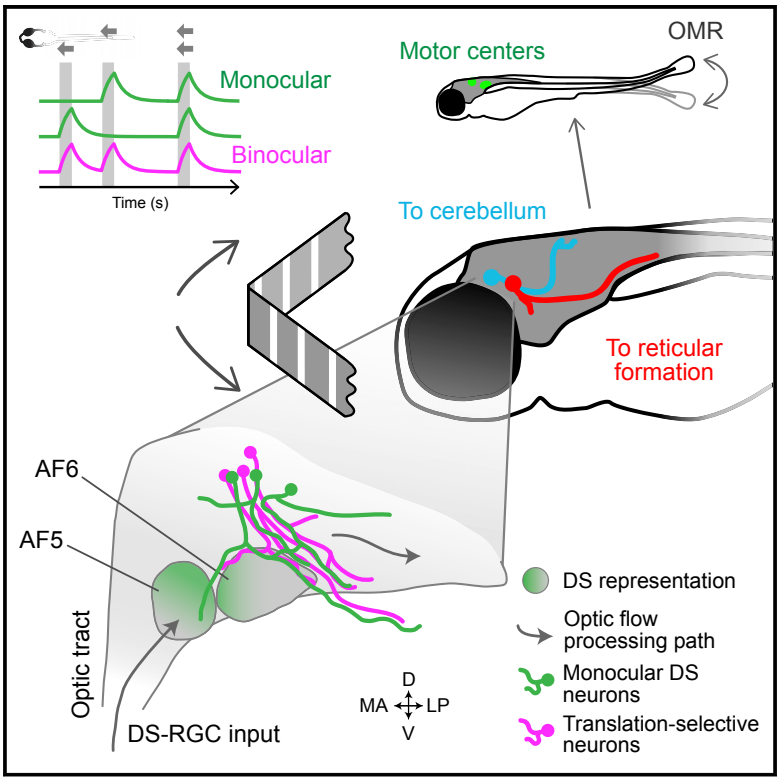

Highlights

- Function-guided inducible morphological analysis (FuGIMA) in pretectum
- Functionally identified, optic-flow-responsive neurons show distinct morphologies
- Direction-selective retinal ganglion cell axons innervate a local pretectal neuropil
- Single-neuron atlas highlights putative optomotor outputs of the pretectal circuit

Authors

Anna Kramer, Yunmin Wu, Herwig Baier, Fumi Kubo

Correspondence

fumikubo@nig.ac.jp

In Brief

Based on the projection patterns of functionally identified neurons in zebrafish pretectum, Kramer et al. propose that monocular direction-selective neurons combine retinal inputs to generate binocular optic flow responses. Single-neuron tracings highlight two downstream pathways to hindbrain motor centers.

Kramer et al., 2019, Neuron *103*, 118–132
July 3, 2019
https://doi.org/10.1016/j.neuron.2019.04.018

CellPress

CellPress

Neuron
Article

Neuronal Architecture of a Visual Center that Processes Optic Flow

Anna Kramer,[1] Yunmin Wu,[1] Herwig Baier,[1] and Fumi Kubo[1,2,3,*]
[1]Department Genes – Circuits – Behavior, Max Planck Institute of Neurobiology, Am Klopferspitz 18, 82152 Martinsried, Germany
[2]Center for Frontier Research, National Institute of Genetics, 1111 Yata, Mishima, Shizuoka 411-8540, Japan
[3]Lead Contact
*Correspondence: fumikubo@nig.ac.jp
https://doi.org/10.1016/j.neuron.2019.04.018

SUMMARY

Animals use global image motion cues to actively stabilize their position by compensatory movements. Neurons in the zebrafish pretectum distinguish different optic flow patterns, e.g., rotation and translation, to drive appropriate behaviors. Combining functional imaging and morphological reconstruction of single cells, we revealed critical neuroanatomical features of this sensorimotor transformation. Terminals of direction-selective retinal ganglion cells (DS-RGCs) are located within the pretectal retinal arborization field 5 (AF5), where they meet dendrites of pretectal neurons with simple tuning to monocular optic flow. Translation-selective neurons, which respond selectively to optic flow in the same direction for both eyes, are intermingled with these simple cells but do not receive inputs from DS-RGCs. Mutually exclusive populations of pretectal projection neurons innervate either the reticular formation or the cerebellum, which in turn control motor responses. We posit that local computations in a defined pretectal circuit transform optic flow signals into neural commands driving optomotor behavior.

INTRODUCTION

When animals actively move, or are passively carried through the environment, their visual systems experience continuous movement of stationary features in the visual scene. Neuronal circuits use the drifting retinal images to compute global image motion (optic flow) in order to adjust the animal's body posture and position and stabilize the direction of gaze. In teleost fish and other vertebrates, the optokinetic response (OKR) and the optomotor response (OMR) are typical optic-flow-driven behaviors that compensate for self-motion (Masseck and Hoffmann, 2009a). Eye movements accompanying the OKR consist of slow following phases, which minimize retinal slip, interspersed by quick reset phases. The OMR is characterized by locomotion in the direction of the perceived motion. This ensures that the animal does not drift away from its location, for instance, in a flowing water stream. Zebrafish larvae older than 5 days post-fertilization (>5 dpf) exhibit both robust OKR and OMR (Neuhauss et al., 1999; Orger et al., 2000, 2004, 2008; Portugues and Engert, 2009; Rinner et al., 2005).

Retinal ganglion cells (RGCs) are the sole output neuron class of the retina. In zebrafish larvae, all RGC axons cross the midline and terminate in nine arborization fields (AFs) (numbered AF1–AF9) in the preoptic area and/or hypothalamus, the thalamus, and the pretectum, in addition to the optic tectum, which is AF10 (Burrill and Easter, 1994; Robles et al., 2014). Each AF and each of the ten layers of the tectum receive input from of a distinct combination of morphologically and functionally identifiable RGC types, which form parallel processing channels for specific visual features, such as prey-like objects, looming stimuli, and decreasing or increasing ambient light levels (Robles et al., 2014; Semmelhack et al., 2014; Temizer et al., 2015; Zhang et al., 2017). A unifying hypothesis posits that behaviorally relevant information is packaged in spatially segregated information channels (Dhande and Huberman, 2014), which in turn evoke distinct adaptive behaviors (Baier, 2000; Helmbrecht et al., 2018). Therefore, knowledge of AF tuning provides a productive entry point to decipher the "division of labor" among the different visual and visuomotor processing streams.

Broad activation of the pretectum (accessory optic system) is sufficient to evoke OKR in mammals and zebrafish, and lesions or experimental inactivation suppress this behavior (Cazin et al., 1980; Kubo et al., 2014; Schiff et al., 1988). This observation led to the prediction that the subset of RGCs that encodes the direction of movement, namely the direction-selective (DS-) RGCs (Barlow and Hill, 1963; Dhande and Huberman, 2014), carries information about image motion to the pretectal area. Previous anatomical work in zebrafish had shown that the RGCs that project to the DS sublayer of the optic tectum, the *stratum fibrosum et griseum superficiale 1* (SFGS1) (Gabriel et al., 2012; Gebhardt et al., 2013; Nikolaou et al., 2012), also form collateral branches in AF5 (Robles et al., 2014). This observation made AF5 a prime candidate for the pretectal neuropil region that receives DS-RGC inputs. Until now, however, DS-RGC responses had not been detected in AF5. Rather, a recent study annotated the neighboring area AF6 as the DS-RGC recipient area (Naumann et al., 2016). One goal of the current study was to precisely map DS-RGC inputs within the pretectum to resolve this discrepancy.

In lateral-eyed animals, such as zebrafish, each eye samples roughly one hemisphere of the visual world. Therefore, integrating visual inputs from both eyes is an obvious strategy for

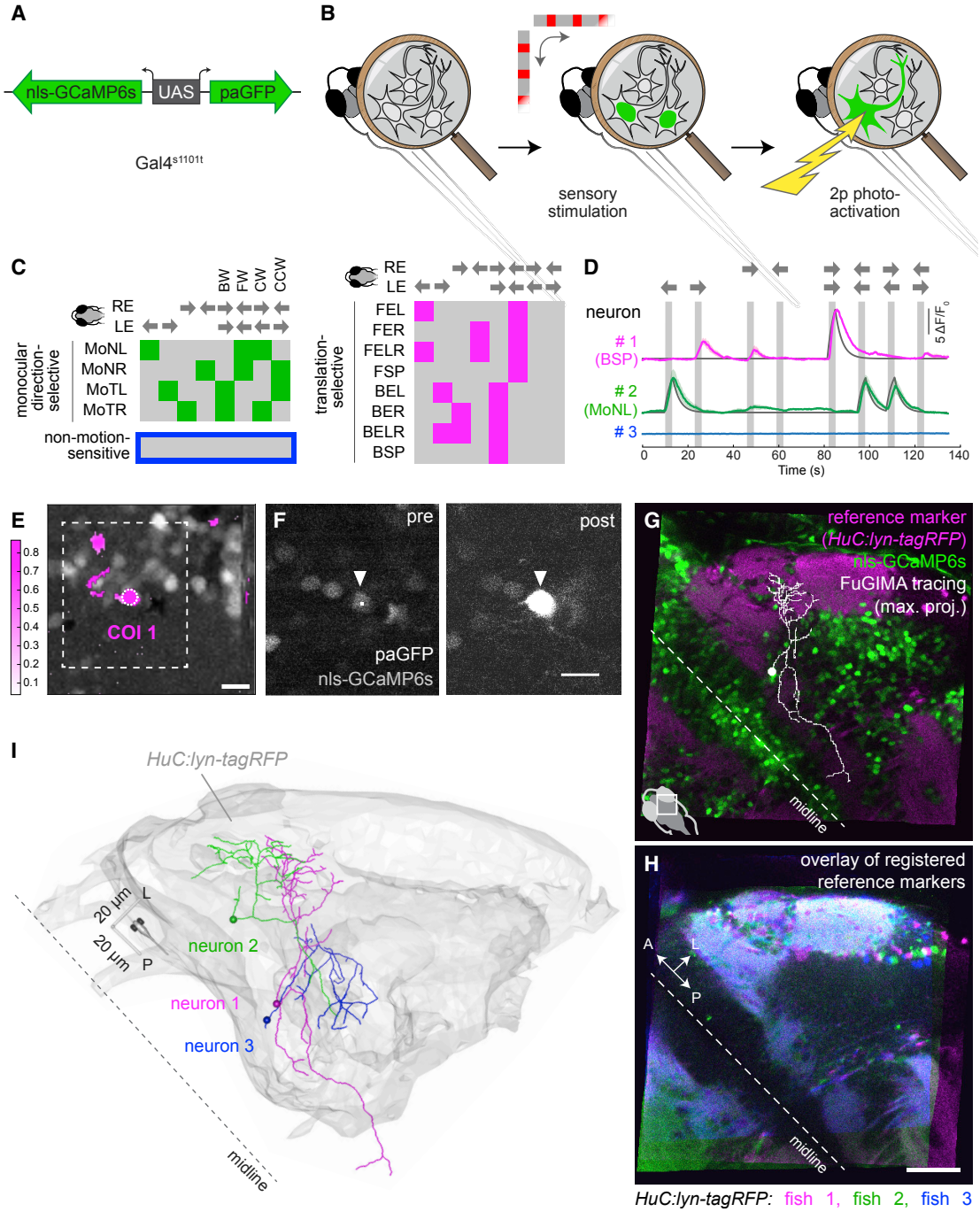

Figure 1. FuGIMA Enables Morphological Reconstructions of Functionally Characterized Pretectal Neurons

(A) The bidirectional genetic construct *UAS:FuGIMA* enables co-expression of nls-GCaMP6s and paGFP using the Gal4-UAS system.

(B) FuGIMA workflow: inactive nls-GCaMP6s and paGFP show little or no fluorescence. During stimulation with horizontally moving gratings, neuronal activity is recorded to determine a cell of interest. PaGFP is focally photoactivated with a two-photon (2p) laser (λ = 750 nm) and subsequently labels the cell of interest's morphology by diffusion.

(C) (Top) The presented visual stimulus consists of eight motion phases, i.e., four monocular (nasalward left, temporalward left, temporalward right, and nasalward right) and four binocular (BW, backward; FW, forward; CW, clockwise; CCW, counter-clockwise) phases (see also Figure S2A). (Below) Of 2^8 possible regressors, the following response types were investigated (barcode visualization): four monocular direction-selective types (green square); eight translation-selective response types (magenta square); and the non-motion-sensitive type (blue outline). Response type names are adapted from Kubo et al. (2014). Filled squares symbolize neuronal activity during the stimulation phase. The color code applies to other panels of this figure. B, backward translation; E, excited by; F, forward translation; L, to the left eye; Mo, monocular; N, nasalward; R, to the right eye; SP, specific; T, temporalward.

(legend continued on next page)

discriminating translational versus rotational optic flow (i.e., movement in the same or in the opposite directions for left and right eye; Masseck and Hoffmann, 2009a, 2009b; Sabbah et al., 2017; Wang et al., 2019; Wylie et al., 1998). Functional imaging had shown that most pretectal neurons in zebrafish fall into one of two broad categories: (1) ''simple'' optic-flow-responsive cells, which are driven by DS inputs from one eye and (2) ''complex'' cells that respond to translational optic flow and are suppressed by rotational optic flow (Kubo et al., 2014). In a parsimonious wiring diagram, simple monocular pretectal cells might combine their DS tuning across hemispheres to generate the responses of complex translation-selective neurons (Kubo et al., 2014). The latter cells might then convey the processed information to premotor centers in the hindbrain, which in turn initiate the OMR.

To test the anatomical predictions of this wiring diagram, we set out to determine the cellular composition of the pretectal optic-flow-processing circuit and test predictions of its input and output pathways. We found that the majority of DS-RGCs terminate in AF5, consistent with earlier anatomical findings (Robles et al., 2014). Morphological reconstructions of optic-flow-responsive pretectal cells showed that the putative dendrites of simple monocular cells overlap with DS-RGC presynaptic terminals in AF5. Complex translation-selective cells have different morphologies and project neurites into a neuropil region abutting, and overlapping with, AF6. Long-range projections connect the optic-flow-sensitive pretectal area to the cerebellum, the reticular formation, and other motor-related centers. Together, our work integrating diverse functional and anatomical datasets traces a universally important visual pathway with cellular resolution from the retina to the hindbrain.

RESULTS

FuGIMA Approach Allows Reconstruction and Visualization of Functionally Identified Pretectal Neurons

We asked how optic flow information is represented by cell types of the pretectum. The pretectum is an anatomically complex region comprised of retinorecipient and non-retinorecipient cells (Yáñez et al., 2018). Pretectal cells with different functional properties are intermingled (Kubo et al., 2014; Naumann et al., 2016). To reveal the morphologies of optic-flow-responsive pretectal neurons, we employed the all-optical method FuGIMA (function-guided inducible morphological analysis) (Förster et al., 2018). FuGIMA is based on the co-expression of nuclear localized GCaMP6s (nls-GCaMP6s) and cytoplasmic photoactivatable GFP (paGFP) under the control of a bidirectional upstream activating sequence (UAS) (Janus-UAS; Distel et al., 2010; Paquet et al., 2009; Figure 1A). Although both nls-GCaMP6s and photoactivated paGFP emit green fluorescence, signals from the two proteins are separated by way of their nuclear versus cytoplasmic localization, thus allowing their combination in the same cell.

We used zebrafish larvae expressing the FuGIMA components in all neurons by crossing the panneuronal driver *Gal4s1101t* with *UAS:FuGIMA* (see STAR Methods). Neuronal activity in the pretectum was recorded by imaging of nls-GCaMP6s signals upon stimulation with whole-field motion (Figure 1B). The visual stimulus protocol consisted of monocular and binocular optic flow patterns (horizontally moving gratings) in a sequence of eight phases: four monocular phases with gratings shown to the left or right side of the fish, moving either nasally or temporally, and four binocular phases, namely backward, forward, clockwise, and counter-clockwise motions (Figure S2A). Responses to each of the eight phases were used to assign to each cell a barcode, which represents the stimulus combination to which the cell is tuned (Kubo et al., 2014; Figure 1C). A cell of interest was then chosen for photoactivation, based on its response to optic flow, and labeled by focusing 750-nm laser light in two-photon (2p) mode onto the soma (Figures 1D–1F). Photoactivated paGFP diffuses into the neurites and, after several hours, reveals the morphology of the cell (Förster et al., 2018; Figure 1G). The maximum distance over which neurites can be traced is dependent on the diffusion properties of paGFP and was empirically determined to be around 200 μm (Figures S1A and S1B; see STAR Methods).

Pretectal Neurons with Optic Flow Tuning Differ in Their Morphologies from Non-Motion-Sensitive Neurons

Out of the 256 (2^8) theoretically possible barcodes, we focused on the following three response classes (Kubo et al., 2014): simple monocular DS (comprising four response types); complex translation-selective (eight response types); and non-motion-sensitive as controls (activity not locked to any motion phase; Figure 1C). We used a regressor-based analysis to semi-automatically identify response types of interest in a near-online fashion (see three exemplary GCaMP6s fluorescent traces in Figure 1D). Among these cells, we selected one cell of interest for photoactivation (correlation map of regressor 1; Figures 1E and 1F). After allowing for diffusion of GFP fluorescence, cells of interest were manually traced (Figure 1G) and registered to a

(D) nls-GCaMP6s fluorescence time series of example neurons of distinct response types identified by regressor-based analysis (overlaid on the respective regressor, gray). Solid colored line, average of three repetitions; shaded area, SEM; gray bars, stimulation periods.

(E) Overlay of field-of-view (mean $\Delta F/F_0$) and pixel-wise regressor-based analysis (color bar: Pearson's correlation coefficient), highlighting two neurons best correlated with the regressor 1 shown in (D) (top trace). The white dotted circle indicates example neuron 1 (COI1, cell of interest 1); white dashed square indicates field of view used in (F).

(F) Photoactivation of neuron 1. Before photoactivation, most nuclei exhibit dim nls-GCaMP6s fluorescence. After photoactivation of the soma, neuron 1 exhibits bright paGFP fluorescence (white arrowhead, neuron 1; small white square, approximate photoactivation region).

(G) Tracing of photoactivated neuron 1 (white, maximum intensity projection) superimposed on one plane of the registered experimental z stack (green, nls-GCaMP6s/paGFP; magenta, *HuC:lyn-tagRFP*).

(H) Overlay of the reference marker (*HuC:lyn-tagRFP*) derived from three experimental fish that have been registered to the standard brain.

(I) 3D rendering of the standard brain surface (gray) with three registered tracings (dorsal view). The color of the three tracings corresponds to that used in (D). Scale bars represent 10 μm in (E) and (F) and 50 μm in (H). See also Figure S1.

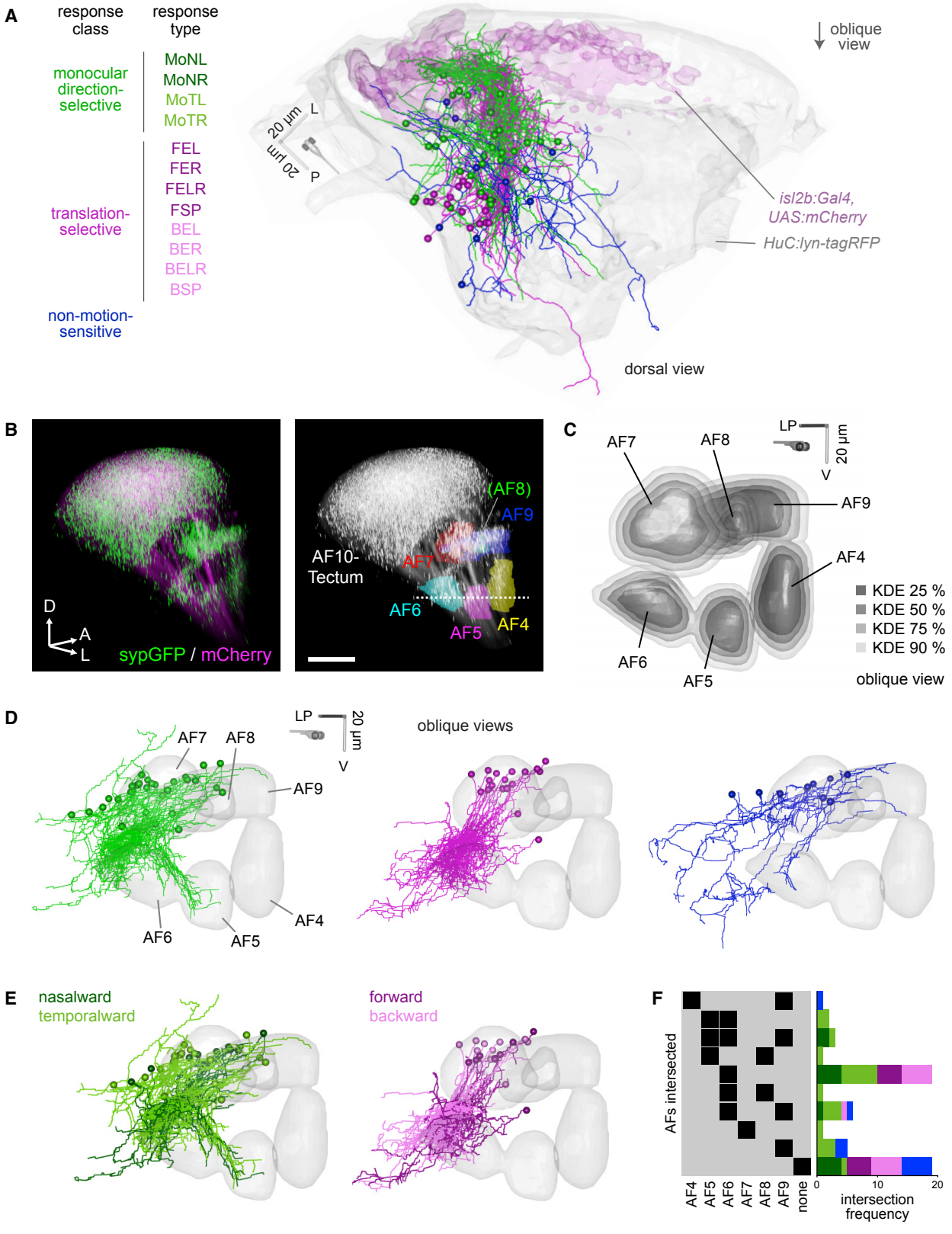

(legend on next page)

standard brain for interindividual comparisons via a reference marker (*HuC:lyn-tagRFP*; Figures 1H, 1I, S1D, and S1E; see STAR Methods).

We reconstructed the morphologies of 58 pretectal neurons from 46 fish (30 monocular DS neurons, 19 translation-selective neurons, and 9 non-motion-sensitive neurons; for individual calcium traces, see Figures S2B and S2C). The respective frequencies of response types detected in our FuGIMA dataset was overall similar to Kubo et al. (2014); however, monocular DS neurons responding to nasalward motion (i.e., MoNR and MoNL) located in the brain ipsilateral to the visually stimulated eye were not identified in this limited dataset (Figures S2D and S2E).

Motion-sensitive neurons in our FuGIMA dataset showed overall similar morphologies; their stem neurite pointed in a lateral-anterior-ventral direction (Figure 2A; Video S1). The neurites of non-motion-sensitive neurons, on the other hand, typically branched and extended in the anterior and posterior directions, suggesting that the morphologies of optic-flow-sensitive cells differ fundamentally from those of the non-motion-sensitive control neurons (Figure 2A). Cell bodies of monocular DS neurons were widely distributed in an anterior-lateral domain, whereas the translation-selective neurons were located in a more confined, posterior-medial domain (Figure S4B).

Neurons with Monocular DS versus Binocular Translational Optic Flow Tuning Differ in Their AF Projection Patterns

To examine which FuGIMA neurons are potentially retinorecipient, we registered RGC axon projections (Figure 2B) to the standard brain (Figures S3A and S3B; see STAR Methods). Guided by known anatomical features (Burrill and Easter, 1994; Robles et al., 2014), the volumes of AFs 4–10 could be reliably annotated (see STAR Methods; Video S2). We found that the majority of optic-flow-responsive cells (35 of 49; 71%) overlapped with one or more of the AFs. We noticed that monocular DS cells (6 of 30; 20%) extended neurites into AF5, regardless of their preferred direction (Figures 2D, left, 2E, left, and 2F; individual tracings in Figure S4A; Video S1), and translation-selective neurons did not receive inputs from the AF5 region. On the other hand, both monocular DS and translation-selective classes densely branch in a region that is abutting, and overlapping with, the dorsal part of AF6. In fact, all translation-selective cells project ventrally in the direction of AF6, regardless of whether they are responsive to forward or backward motion (Figures 2D, middle, and 2E, right).

The analysis of intersections of all FuGIMA tracings with AF boundaries (defined by kernel density estimate [KDE] = 50%) revealed that many FuGIMA cells (25 of 58; 43%) intersected with one AF: 19 with AF6; 5 with AF9; and 1 with AF7. About a quarter of FuGIMA-traced cells (14 of 58; 24%) intersected with more than one AF in varying combinations (Figure 2F). The total number of intersections per AF changed with the applied threshold for KDE. However, as we varied KDE from 25% to 75%, the number of cells overlapping with AFs 5, 7, and 8 remained constant (n = 6, 1, and 2, respectively), suggesting that overall intersection patterns of response classes do not depend on the stringency with which these AFs are annotated (Figure S3C).

DS-RGCs Project to Pretectal Neuropil Area AF5

Monocular DS-responsive pretectal neurons may inherit their tuning from DS-RGCs that project to AF5. To test this prediction, we measured responses to moving gratings in RGC axon terminals and aligned the functional responses from multiple fish in a second standard brain, "RGC standard brain," which we constructed based on the *isl2b:Gal4* × *UAS:mCherry* labeling pattern (Figure S5A). The *isl2b* promoter allows targeting of the vast majority of RGCs (Pittman et al., 2008), and DiI injection confirmed that the *isl2b:Gal4* line labels most of the RGCs terminating in the ventrally located AF4–AF6 (Figure S5E). For imaging of axon terminals of DS-RGCs in the pretectum, we expressed synaptophysin-tagged GCaMP6s (syGCaMP6s) in RGCs (*isl2b:Gal4; UAS:syGCaMP6s*; Figures S5B-S5D). Fusion to synaptophysin targets the calcium indicator to presynaptic terminals (Dreosti et al., 2009; Dunn et al., 2016; Nikolaou et al., 2012). Recorded syGCaMP6s signals were then mapped onto the RGC standard brain (see STAR Methods), and accuracy of the mapping was confirmed by overlay of multiple brains with the RGC standard brain (Figures S5F–S5K).

We examined visual motion-induced activity in RGC terminals by presenting monocular moving gratings to the contralateral eye of the fish. Visual stimuli were presented from the side of the fish, and recorded brain areas included most of the tectal neuropil (AF10) and more ventral AFs in the pretectum and thalamus, including AF4–AF6 (Figures 2B and 3A). Response profiles of AF4 and AF6 were largely consistent with previous studies, with AF4 being activated by ON and AF6 by OFF whole-field luminance changes (Temizer et al., 2015; Zhang et al., 2017;

Figure 2. Monocular DS and Translation-Selective Neurons Show Different Morphologies

(A) 3D rendering of all FuGIMA tracings (n = 58 tracings) with the standard brain (*HuC:lyn-tagRFP*) and RGC terminals as labeled with *isl2b:Gal4, UAS:mCherry*. The tracings are color coded according to the neurons' response class (dorsal view). See also Video S1.

(B) Anatomical representation of AFs. (Left) SypGFP signal driven by *atoh7:Gal4* driver reveals distinct AFs at 6 dpf (compound of three fish). (Right) Annotation of AFs in the same 3D volume is shown. Dotted line corresponds to the optical planes for imaging AF4, AF5, and AF6. See also Video S2.

(C) Boundaries of AFs (from the RGC standard brain) after registration to the FuGIMA standard brain. 3D rendering of a thresholded kernel-density estimation (KDE) of co-registered AF masks from (B) (thresholded to 25%, 50%, 75%, and 90%; n = 7 bridging z stacks, from 4 fish). See also Figure S3.

(D) 3D rendering of FuGIMA tracings grouped by response class together with AF masks (oblique views; AFs 4–9; KDE = 50%).

(E) Further classification of FuGIMA neurons by direction selectivity (left: light green, monocular temporalward; dark green, monocular nasalward. right: light magenta, backward; dark magenta: forward).

(F) Analysis of morphological types of all FuGIMA neurons. Intersections of individual tracings with AFs 4–9 reveals widespread intersections between FuGIMA tracings and the AFs (black squares symbolize the intersection with the indicated AF). (Right) Intersection frequency according to response class is shown. Scale bar represents 50 μm in (B). See also Figures S2, S3, and S4.

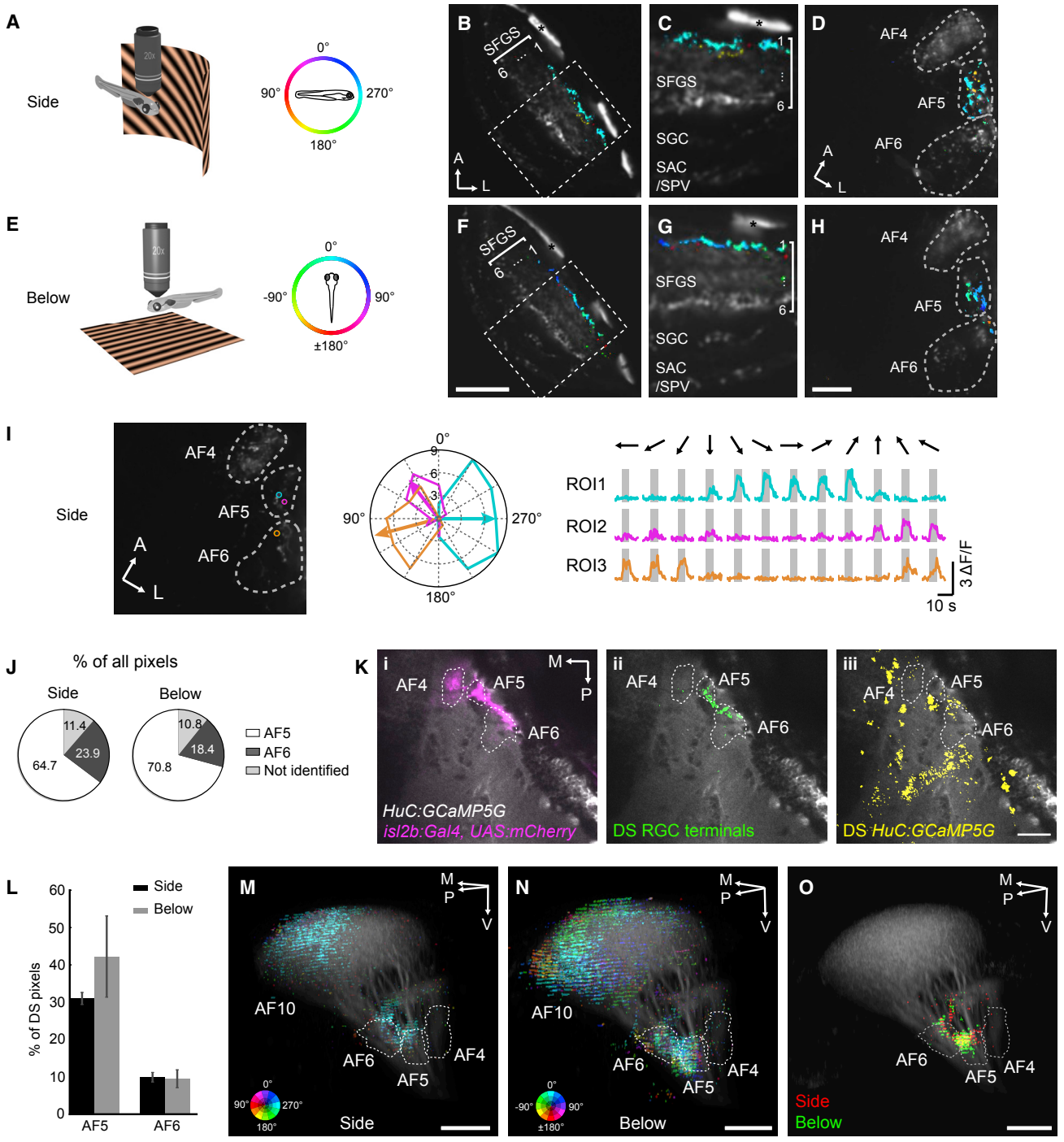

Figure 3. Direction-Selective RGCs Largely Terminate in Arborization Fields AF5 and Tectum (AF10)

(A) Schematic of the experimental setup for visual stimulation with moving gratings presented from the side. Color indicates direction of motion.

(B–D) DS pixels in AF10 (B and C) and AF4, AF5, and AF6 (D).

(E) Schematic of the experimental setup for visual stimulation with moving gratings presented below.

(F–H) DS pixels in AF10 (F and G) and AF4, 5, and 6 (H). In (B)–(D) and (F)–(H), DS pixels are plotted on top of the mean image of syGCaMP6s (gray).

(I) Representative responses of DS-RGC terminals in AF5 and AF6. Visual stimuli were presented from the side. ROIs correspond to synaptic puncta marked in the left image. Polar plot (middle) is derived from the ΔF/F traces shown on the right.

(J) Distribution of DS pixels identified in ventral AFs. The pie charts show the percentage of DS pixels residing in AF5, AF6, and a region neither AF5 nor 6 ("not identified"), summed from 6 and 7 fish for side and below stimulus presentation, respectively.

(legend continued on next page)

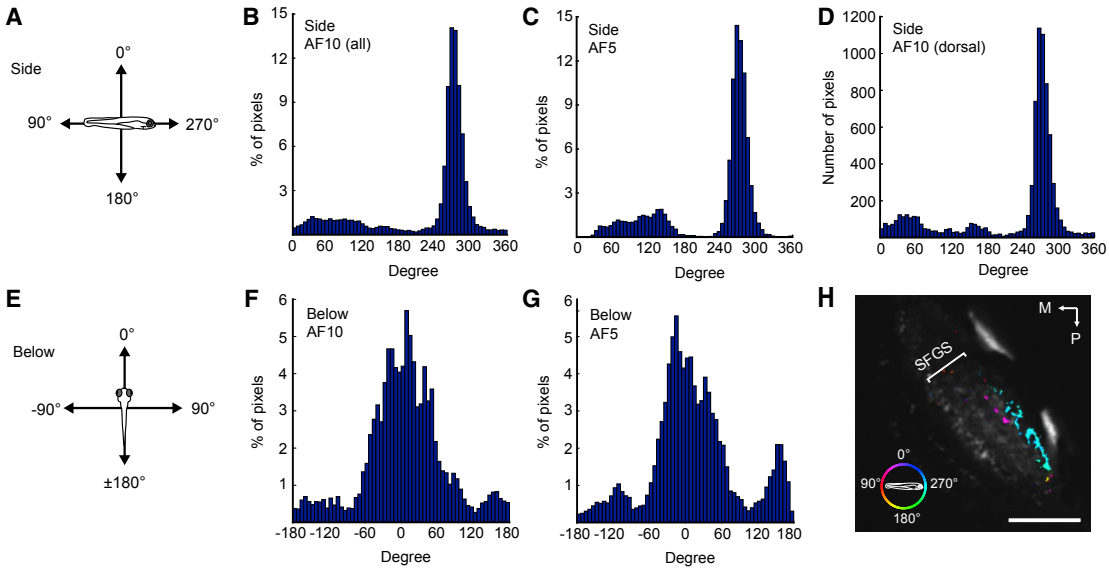

Figure 4. Distribution of Preferred Directions of DS-RGCs Reveals Shared Inputs in AF5 and Tectum

(A) Direction space of motion stimulus presented from the side.

(B and C) Distributions of preferred directions of DS-RGC terminals in AF10 (B; N = 6 fish) and AF5 (C; N = 6 fish). Motion was presented from the side.

(D) Distribution of preferred direction of DS-RGC terminals in the dorsal AF10. In contrast to (B), where the entire AF10 was sampled, only 3 planes (separated by 4 μm) in AF10 were selected in this histogram, as was reported previously (Nikolaou et al., 2012).

(E) Direction space of motion stimulus presented from below.

(F and G) Distributions of preferred directions of DS-RGC terminals in AF10 (F; N = 7 fish) and AF5 (G; N = 7 fish). Motion was presented from below.

(H) DS response map of a single representative optical plane in the dorsal AF10 analyzed in (D). Scale bar: 30 μm.

Figures S6A–S6C). We then identified pixels that exhibited DS signals ("DS pixels"; see STAR Methods). Within the tectum, DS pixels localized to the posterior half of the SFGS1 (Figures 3B, 3C, S6D, and S6E), as described previously (Nikolaou et al., 2012). In a more ventral optical plane, DS pixels were found predominantly in AF5 (64.7%), with fewer DS pixels in AF6 (23.9%; N = 6; Figures 3D and 3J). This difference was further augmented when the relatively larger number of synaptic puncta within AF6 were considered. DS pixels represented about 30%–40% of the total pixels in AF5, whereas in AF6, the DS pixels comprised about 10% of the total pixels (Figure 3L). The responses localized to AF6 by our anatomical mask were observed in terminals close to the boundary to AF5, suggesting that the corresponding terminals might sit on branches of AF5-projecting RGCs (Figures 3D and 3I). In addition, a sparse subset of RGC terminals in AF6 was orientation selective (OS) (Figures S6F–S6J). In conclusion, the majority of the DS-RGC inputs are sent to AF5.

AF5 (and SFGS1) Receive Retinal DS Responses Regardless of RGC Soma Position within the Retina

In a previous study (Naumann et al., 2016), motion stimuli were presented from below, which activates predominantly the dorsal part of the retina (Robles et al., 2014; Stuermer, 1988). It is conceivable that dorsally positioned DS-RGCs project to different AFs than those that were activated by motion shown from the side. To test this possibility, we repeated above imaging experiments while displaying moving gratings from below

(K) Overlay of a registered *HuC:GCaMP5G* image (gray) with RGC axons (i, *isl2b:Gal4, UAS:mCherry*), DS-RGC terminals (ii, identified from below projection; sum of 6 fish), and DS neuropil of *HuC:GCaMP5G* fish (iii, identified from below projection; sum of 5 fish) in an optical plane that contains AF4, AF5, and AF6. DS-RGCs and DS neuropil represent all DS populations tuned to any direction of motion.

(L) Percentage of DS pixels relative to the entire pixel counts in AF5 and 6. Average pixel counts in each AF were quantified using anatomical stacks of *isl2b:Gal4, UAS:sypGFP* fish (see STAR Methods for details). N = 6 fish (side) and 7 fish (below) for each AF. Error bars represent SEM.

(M and N) 3D representations of DS-RGC terminals. For side-presented 3D map (M), both AF10 and AF4, AF5, and AF6 volumes are pooled from 6 imaged volumes. For below-presented 3D map (N), both AF10 and AF4, AF5, and AF6 volumes are pooled from 7 imaged volumes. Color wheels represent the preferred directions of DS pixels. The intensity of DS pixels corresponds to the probability of a particular pixel to be DS across all imaged fish (the maximum intensity corresponds to the frequency of 0.67 and 0.57 for M and N, respectively). See also Videos S3 and S4.

(O) Comparison of DS-RGC terminals responsive to side versus below presentations. Composite 3D map of a single fish that underwent both side and below presentations. Note that DS-RGC terminals identified by side (red) and below (green) presentations co-localize in AF5. A, anterior; L, lateral; M, medial; P, posterior; SAC, *stratum album centrale*; SFGS, *stratum fibrosum et griseum superficiale*; SGC, *stratum griseum centrale*; SPV, *stratum periventriculare*; V, ventral; *, skin auto-fluorescence.

Scale bars represent 20 μm (F), 10 μm (H), 30 μm (K), and 50 μm (M–O). See also Figures S5 and S6.

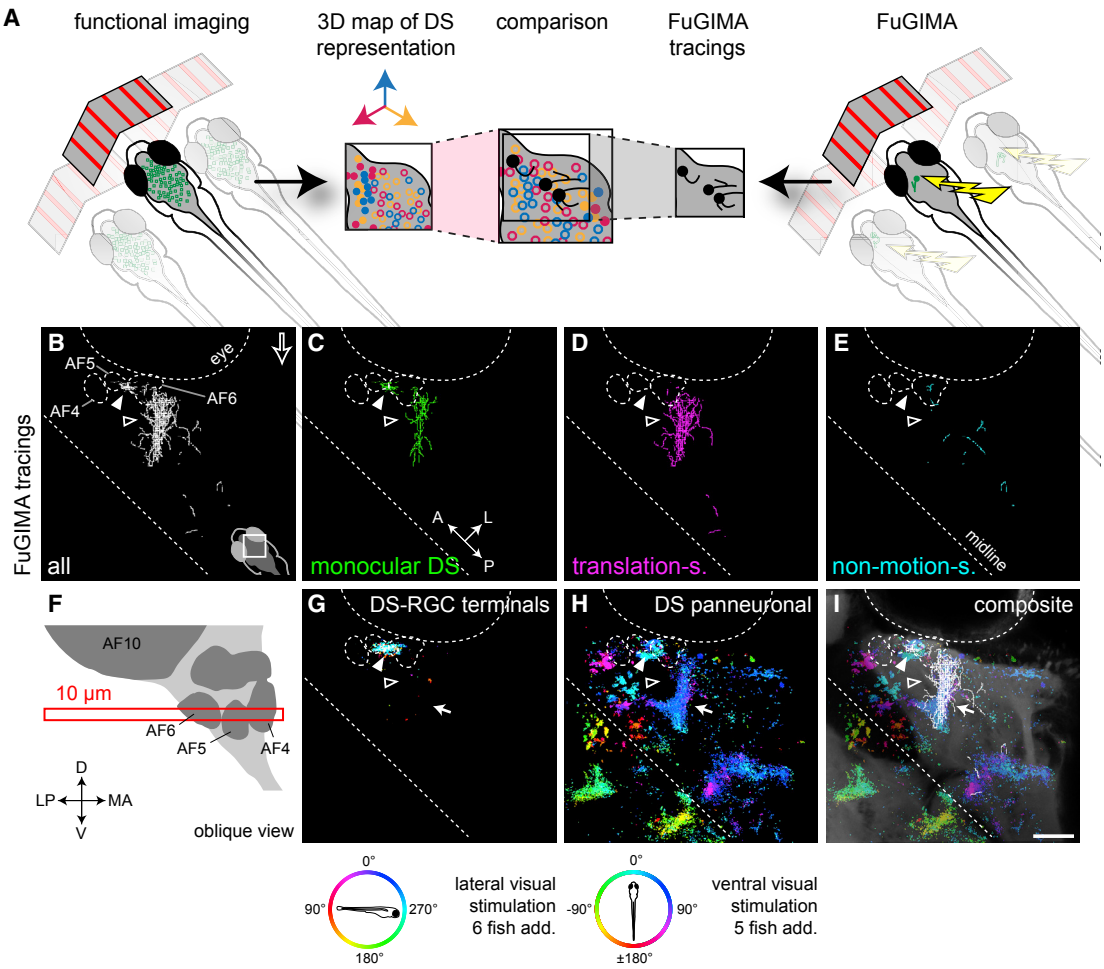

Figure 5. Co-registration of FuGIMA with Two Functional Imaging Datasets Shows Overlap of DS-RGC Input with Monocular DS, but Not with Translation-Selective, Neurons

(A) Schematic illustrating acquisition and integration of the functional maps and the FuGIMA dataset.

(B–I) A slice of the co-registered volume at the level of the AFs 4–6 with FuGIMA tracings and functional maps of DS-RGC terminals and DS neurons (right hemisphere, maximum intensity projection over z = 10 µm; see schematic in F; of 58 FuGIMA tracings, 42 of the following classes extend into the slice: 19 monocular DS; 17 translation-selective; 6 not motion-sensitive).

(B–E) FuGIMA tracings (open white arrowhead, FuGIMA tracing bundle; filled white arrowhead, small tracing patch at the border between AFs 5 and 6; open arrow, direction of oblique view): (B) all (white); (C) monocular DS (green); (D) translation-selective (magenta); and (E) non-motion-sensitive (blue).

(F) Schematic of z stack slicing (oblique view used to visualize optic tract [light gray] and AFs [dark gray]).

(G) Registered 3D map of DS-RGC terminals (*isl2b:Gal4, UAS:syGCaMP6s*; see color wheel below for direction of moving gratings presented from side; composite of 6 fish).

(H) Registered 3D map of DS-panneuronal (*HuC:GCaMP5G*; white arrow, broad band of DS pixels; see color wheel below for direction of moving gratings presented from below; composite of 5 fish).

(I) Composite of DS-panneuronal with all FuGIMA tracings and standard brain reference marker (*HuC:lyn-tagRFP* in gray).

For (G)–(I), imaging artifact DS pixels located in the eye were removed with a mask. Scale bar represents 50 µm (I).

(Figures 3E–3H). Similar to the presentation from the side, the majority of DS-RGC inputs were found in AF5 (70.8%), and fewer were found in AF6 (18.4%; N = 7 fish; Figure 3J). DS-RGC inputs from dorsal retina were also observed in SFGS1 (Figures 3F, 3G, S6D, and S6E). This indicates that DS-RGCs project to AF5 and SFGS1, regardless of their soma positions along the dorsoventral axis of the retina.

To localize DS-RGC pixels within the larger neuropil volume surrounding the AFs, we registered an image stack from the *HuC:GCaMP5G* line to our RGC standard brain. As expected, RGC axons occupied only a small subvolume of the pretectal neuropil labeled in *HuC:GCaMP5G* (Figure 3Ki). Registration of visual responses to whole-field motion in the RGC standard brain revealed that DS responses in the panneuronal *HuC:GCaMP5G* neuropil extended outside of the AFs (Figures 3Kii and 3Kiii).

To establish a 3D map of DS representations in RGC terminals, we mapped DS pixels identified in multiple fish onto the RGC standard brain. In the tectum, DS pixels occupied the posterior

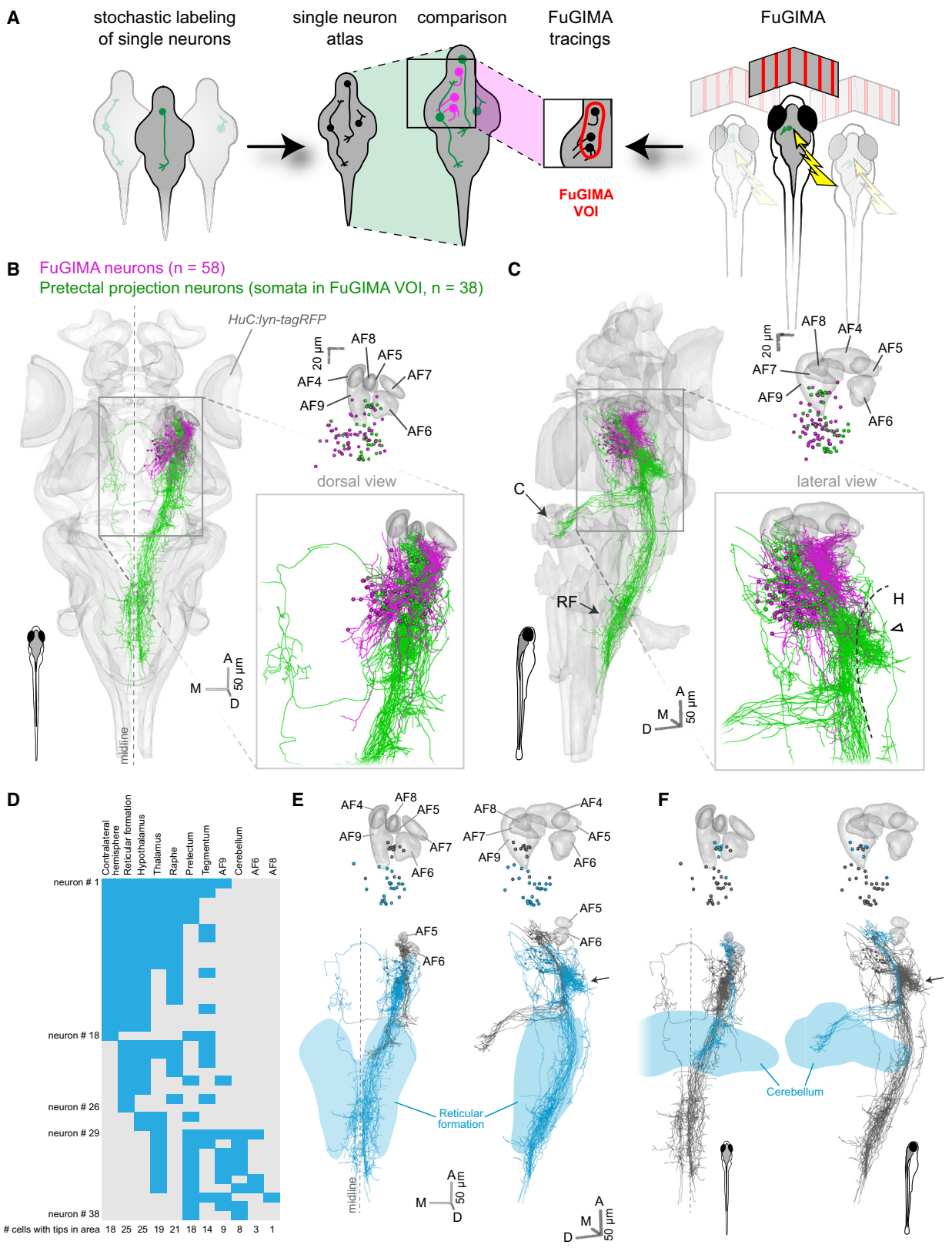

(legend on next page)

half of the neuropil volume when the stimulus was presented from the side (Figure 3M; Video S3). When the stimulus was projected from below, DS pixels were preferentially identified in the ventral tectum (Figure 3N; Video S4). This location is consistent with the topographic organization of the retinotectal projection (Robles et al., 2014; Stuermer, 1988). Notably, in the pretectum, a co-registration of DS pixels obtained from a single fish, which was stimulated both from the side and from below, shows that the identified DS pixels were co-localized in a similar volume, corresponding to AF5 (Figure 3O). In summary, our results demonstrate that RGC terminals exhibiting DS responses in the pretectal neuropil are situated predominantly in AF5 and that this is independent of the position of the visual stimulus.

AF5- and SFGS1-Projecting DS-RGCs Show Very Similar DS Tuning, Consistent with Collateral Branching from the Same Axon

We hypothesized that the DS-RGC axon terminals in AF5 are collateral branches of RGCs projecting to SFGS1. If so, preferred directions of RGC axons in AF5 should be identical to those in SFGS1. When the visual stimuli were presented from the side (Figures 4A–4D and 4H), the majority of the DS pixels were tuned to forward stimulus motion (~270°) in both the tectum (Figure 4B) and AF5 (Figure 4C), with a much smaller population of DS pixels with broadly distributed preferred directions between 30° and 180°. In the dorsal part of the tectum, we observed three populations of DS-RGCs, tuned to whole-field motion in a forward (270°), oblique-backward (around 45°), and downward (around 160°) direction, respectively, as reported previously (Lowe et al., 2013; Nikolaou et al., 2012; Figures 4D and 4H). When the visual stimuli were presented from below, the majority of DS pixels in SFGS1 and AF5 preferred the forward direction (~0°) as well (Figures 4E–4G). These results are in agreement with a direction-of-motion-sensitive visual pathway composed of three differently tuned classes of DS-RGCs, whose axons branch in AF5 on their way to SFGS1.

DS-RGC Terminals Spatially Overlap with Dendrites of Monocular DS-Pretectal Cells in AF5

We next tested the prediction that the neurites of monocular DS pretectal neurons coincided in space with DS-RGC terminals. In FuGIMA experiments, calcium responses in the neuropil are invisible due to nuclear localized GCaMP. Therefore, we registered two sets of functional imaging data to the FuGIMA standard brain: DS signals recorded in RGC terminals (*isl2b:Gal4*, *UAS:syGCaMP6s*) and DS signals from all neurons (*HuC:GCaMP5G*; Figure 5A). In this overlay, DS-RGC pixels overlapped with dendrites from monocular DS cells, but not with those of translation-selective neurons (Figure 5G). Neurites of both monocular DS and translation-selective cells were also seen outside the RGC neuropil, caudal to AF6 (Figures 5B–5D). This region was contained in the broader pretectal DS neuropil revealed by *HuC:GCaMP5G* imaging (Figures 5H and 5I). Tracings of control neurons (non-motion-sensitive) did not overlap with DS-RGC pixels (Figure 5E). Taken together, registration of two 3D maps of functional data to the FuGIMA dataset suggests that monocular DS neurons receive direct input from DS-RGCs in AF5 and that additional DS responses in the pretectum emanate from branches of pretectal optic-flow-responsive neurons.

Distinct Classes of Pretectal Neurons from the Optic-Flow-Processing Region Project to Premotor Centers

We hypothesized that translation-selective neurons might project to premotor centers that drive the OMR. The FuGIMA method relies on relatively slow, distance-dependent diffusion of paGFP and is therefore unsuited to label long-range projections. To investigate the connections of the DS pretectal area, we employed "virtual tract tracing" by interrogating the cellular-resolution brain atlas of Kunst et al. (2019) [this issue of *Neuron*]. At the time of analysis, this dataset contained the morphologies of 1,743 single-cell tracings, all co-registered within a standard brain. Specifically, we focused on pretectal projection neurons (PPNs) whose cell bodies reside in immediate vicinity of FuGIMA neurons (Figure 6A).

38 PPNs were found to reside within the cloud-shaped "FuGIMA volume of interest" (FuGIMA VOI) (offset between cell body center and edge of volume ~10 μm; Figure S7A). Cell bodies of these neurons (Figure S7B) tend to be located laterally compared to those of the FuGIMA neurons (Figure 6B). Axons of PPNs terminate in the hindbrain reticular formation (25 "pretecto-reticular" PPNs; 18 = 72% thereof in the contralateral hemisphere) or the cerebellum (8 "pretecto-cerebellar" PPNs) in a mutually exclusive pattern (Video S5). A large fraction of neurons also terminate in the hypothalamus (25 of 38), the thalamus (19 of 38), the raphe (21 of 38), the pretectum (18 of 38), and tegmentum (14 of 38; including the nucleus of the medial longitudinal fascicle, the oculomotor nucleus, and the nucleus isthmi), in various combinations. AFs encompassing PPN termini are AF9 (9 of 38), AF6 (3 of 38), and AF6 (1 of 38). The cell bodies

Figure 6. Pretectal Projection Neurons Target the Cerebellum and Ventral Hindbrain

(A) Schematic illustrating the strategy to combine the single-neuron atlas of Kunst et al. (2019) and the FuGIMA dataset.

(B and C) 3D representation of the standard brain (*HuC:lyn-tagRFP*) together with all FuGIMA neurons (magenta, n = 58) as well as pretectal projection neurons (PPNs) (green, n = 38), chosen based on their soma location within the FuGIMA "volume-of-interest" (FuGIMA VOI) (Figure S7).

(B) (Left, dorsal view, top right) Dorsal view of cell bodies with AFs 4–9; (bottom right) detail of tracings.

(C) As (B) but lateral view (C, cerebellum; H, hypothalamus; RF, reticular formation; dashed line, dorsal border of hypothalamus; open arrowhead, dense branching of PPNs).

(D) Intersection analysis of PPNs with annotated brain areas, i.e., contralateral hemisphere, reticular formation, hypothalamus, thalamus, raphe, pretectum, tegmentum, AF9, cerebellum, AF6, and AF8. Each row represents one neuron; blue filled rectangles symbolize intersection with the annotated brain area.

(E) 3D rendering of intersection of PPNs with the reticular formation (blue, intersecting tracings [n = 25 of 38 PPNs]; gray, not intersecting PPNs; light blue, reticular formation; top, somata and AFs 4–9; bottom, tracings and AFs 5 and 6; left, dorsal view; right, lateral view; arrow, dense branching area in dorsal hypothalamus).

(F) As (E) but intersection of PPNs with the cerebellum (blue, intersecting tracings [n = 8 of 38 PPNs]; light blue, cerebellum).

See also Figure S7 and Video S5.

of pretecto-reticular PPNs reside in the posterior-lateral part of the FuGIMA VOI (Figure 6E). Their axons heavily branch in an area directly posterior and about 20 μm ventral to the main branching area of FuGIMA cells, partially crossing the dorsal border of the hypothalamus (Figures 6C and 6E). Most of them (18 of 25) project bilaterally (Figures 6D and 6E). In contrast, cell bodies of the pretecto-cerebellar PPNs were mainly found in an anterior cluster lateral to AF9 (Figure 6F). Their neurites branch in the vicinity of the cell body, contacting AF6 (n = 2), or AF9 (n = 5), again in varied combinations, and terminate in two patches of the medial cerebellum (Figures 6D and 6F). The traced set of PPNs did not intersect with AF4, AF5, or AF7. In conclusion, two mutually exclusive groups of PPNs connect the optic-flow-sensitive region to the reticular formation (often with collaterals in the hypothalamus) and to the cerebellum (often with collaterals in thalamus and pretectum).

DISCUSSION

This study has revealed the cellular composition, as well as the afferent and efferent pathways, of the optic-flow-processing center in the zebrafish pretectum. We demonstrate that signals from DS-RGCs are transmitted primarily to retinal arborization field AF5 in the pretectal neuropil. DS-RGC axon terminals spatially overlap with putative dendrites of simple, monocular DS pretectal neurons in AF5, but not with those of complex, translation-selective neurons. Complementation of the FuGIMA dataset with tracings from a single-neuron atlas has revealed projection targets of pretectal neurons, i.e., the reticular formation, the tegmentum, the hypothalamus, and the cerebellum. Based on our findings, we propose a model of processing stages in the optic-flow-responsive pathway (Figure 7). Direction selectivity, transmitted by RGC axons to AF5, is inherited by simple, monocular DS neurons and is then combined across the two eyes, likely in the densely innervated neuropil dorso-posterior to AF6, to generate translation-selective tuning in complex cells. The behaviorally relevant binocular optic flow information, computed in the pretectum, is then further relayed to premotor areas in the hindbrain to ultimately drive optomotor behavior.

We demonstrate that DS-RGCs project mainly to AF5. A smaller fraction of DS-responsive RGC terminals was also found in AF6. It is noteworthy that, to generate the consensus anatomical mask, AF boundaries were drawn by outlining the silhouettes of neuropil shapes in multiple fish. Functional data were not taken into consideration in these AF annotations, and it is conceivable that axon collaterals do not respect our annotated anatomical boundaries. It is plausible that the DS responses detectable in AF6 originate from branches of RGC axons that are primarily targeting AF5. This interpretation is in contrast to a previous study (Naumann et al., 2016), which implicated AF6 in pretectal DS-RGC processing. Naumann et al. (2016) identified a conglomerate of neuropil areas exhibiting DS responses as "AF6." The fish they imaged carried the *HuC:GCaMP5G* transgene, in which GCaMP is expressed in almost all neurons. Because GCaMP expression was therefore not limited to RGCs, this approach does not differentiate AFs or disambiguate RGC terminals from axons or dendrites that arise from other neurons. When we registered our two imaging datasets performed in *HuC:GCaMP5G* transgenic fish and RGC terminals into the FuGIMA dataset, the DS neuropil area detected in *HuC:GCaMP5G* transgenic fish overlaps with both RGC terminals and neurites of motion-responsive pretectal neurons. This result suggests that Naumann et al.'s AF6 is likely a mix of AF5, AF6, and additional neuropil formed by pretectal neurons; it is certainly not exclusively AF6.

A previous comprehensive analysis of projection patterns of RGC axons revealed that AF5-projecting RGCs do not form collaterals in AF6 and vice versa (Robles et al., 2014). Furthermore, all AF5- and AF6-projecting RGCs in addition innervate specific layers of the tectum. AF6-projecting RGCs innervate the deepest layer of the SFGS (SFGS6) and the *stratum griseum centrale* (SGC) (Robles et al., 2014), which do not show DS responses (Gabriel et al., 2012; Nikolaou et al., 2012). AF5-projecting RGCs, on the other hand, innervate the most superficial layer of the SFGS layer (SFGS1), which receives DS-RGC input (Gabriel et al., 2012; Nikolaou et al., 2012; this study). Assuming that multiple axonal branches of single DS-RGCs share the same tuning, our functional imaging result is therefore consistent with the anatomical organization of RGC projection patterns, further supporting AF5 as a center for DS motion processing.

We applied the FuGIMA technique (Förster et al., 2018) to tie tuning properties of individual neurons to their morphologies. This method is based on diffusion of the fluorescent paGFP and is therefore well suited to label local neurites, particularly dendrites, whose calibers are generally bigger than those of axons (Vishwanathan et al., 2017) but cannot be used to trace axons over long (>200 μm) distances. We focused on monocular DS neurons, i.e., neurons that respond to movement detected by the contralateral eye, located in the anterior medial cluster of the pretectum, as reported before (Kubo et al., 2014). Ipsilateral monocular DS neurons, which were present in the much larger dataset of Kubo et al. (2014), are missing in our FuGIMA dataset (Figure S2E). We suspect that this discrepancy is rooted in the different transgenic lines used (*HuC:GCaMP5G* by Kubo et al., 2014 and $Gal4^{s1101t}$ × *UAS:FuGIMA* in this study, respectively).

We hypothesized that at least a subset of the translation-selective pretectal cells might be projection neurons (PPNs), which convey information to the premotor centers that drive the OMR. Activity in the reticular formation and the tegmentum has been shown to be correlated with forward swimming and/or turning behavior (Chen et al., 2018; Naumann et al., 2016; Portugues et al., 2014; Vladimirov et al., 2018). Another potential recipient of optic-flow-related information from the pretectum is the cerebellum. Previous work described cerebellar tuning to whole-field motion in cerebellar granule and Purkinje cells (Knogler et al., 2017; Matsui et al., 2014). Purkinje cells in the medial part of the cerebellum were active during OMR, whereas the lateral part was active during the OKR (Matsui et al., 2014). We interrogated a single-neuron atlas (Kunst et al., 2019) to search for PPNs whose cell bodies reside in the optic-flow-responsive region. Most PPNs from this dataset send axons to either of two targets, the reticular formation or the cerebellum. In addition, many PPN axons form collateral branches in the hypothalamus, thalamus, raphe, pretectum, and tegmentum. A mutually exclusive innervation of cerebellum and reticular formation by pretectal efferents has also been reported for adult zebrafish (Yáñez

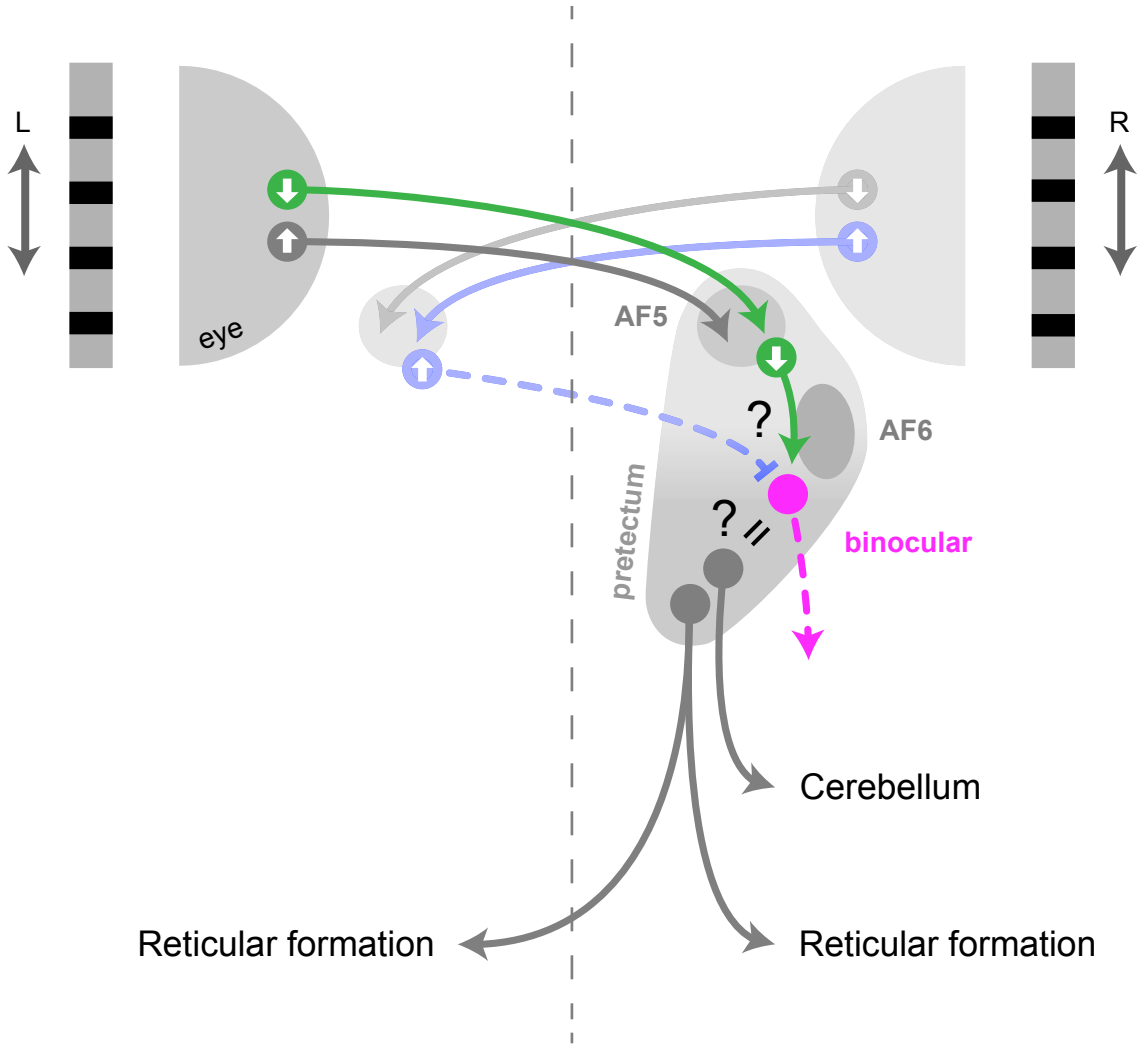

Figure 7. Model for the Optic-Flow-Processing Pathway

The majority of pretectal DS-RGCs terminate in AF5, where they likely synapse onto simple monocular DS neurons. Monocular DS neurons project to a neuropil region within the pretectum, close to the dorsal edge of AF6, where they overlap with translation-selective neurons. Binocularity can be established via inhibition by predicted commissural monocular DS neurons. Information about translational optic flow is transmitted by mutually exclusive populations of pretectal projection neurons to premotor centers either in the cerebellum or in the reticular formation, together evoking directed optomotor responses.

et al., 2018). The PPNs that we describe here are not characterized functionally. However, 10 out of 38 PPNs arborize in AF6, 8, or 9, which some of the FuGIMA-reconstructed neurons also innervate, suggesting that a subset, if not all, of the PPNs correspond to optic-flow-responsive cells that we analyzed with FuGIMA. Binocular integration depends on interhemispheric transfer of DS information (Kubo et al., 2014; Naumann et al., 2016). Interestingly, when we scanned the single-cell atlas anterior to the FuGIMA volume, we discovered a population of commissural neurons in the pretectum that might subserve this function (unpublished data). Commissural neurons projecting to the contralateral pretectum have been described in adult zebrafish (Yáñez et al., 2018).

In conclusion, our results identify a cell-resolved retina-pretectum-hindbrain pathway of the optic flow computation underlying the OMR. A combination of functional and anatomical approaches can offer a unique opportunity to gain new insights into neural circuits that cannot be obtained by a single approach alone. Our circuit model provides a blueprint for the identification of synaptic connectivity and circuit mechanisms underlying optic flow processing in the vertebrate brain.

STAR★METHODS

Detailed methods are provided in the online version of this paper and include the following:

- KEY RESOURCES TABLE
- CONTACT FOR REAGENT AND RESOURCE SHARING
- EXPERIMENTAL MODEL AND SUBJECT DETAILS
  - Animal care and transgenic zebrafish
  - Line establishment
- METHOD DETAILS

SUPPLEMENTAL INFORMATION

Supplemental Information can be found online at https://doi.org/10.1016/j.neuron.2019.04.018.

A video abstract is available at https://doi.org/10.1016/j.neuron.2019.04.018#mmc8.

ACKNOWLEDGMENTS

We thank Irene Arnold-Ammer for plasmid construction, Estuardo Robles for advice on the annotations of RGC arborization fields, Marco Dal Maschio for assistance with 2p microscopy, Thomas Helmbrecht and Vilim Štih for writing code enabling fast regressor-based analysis of functional imaging time series, Michael Kunst for advice on image registration with ANTs and sharing of the single-neuron database prior to publication, Nouwar Mokayes for programming, Aristides B. Arrenberg and agency Prudenter Agas for illustrations of the visual stimulation setup, the entire Baier lab for constructive feedback throughout the project, the Max Planck Computing and Data Facility in Garching for processing the image registration, and the staff of the MPIN fish facility for outstanding fish care. Funding was provided by the Max Planck Society (all authors) and the DFG Priority Programme "Computational Connectomics" (SPP 2041; F.K.).

AUTHOR CONTRIBUTIONS

H.B. and F.K. conceived the project. A.K. performed FuGIMA experiments, generated the *UAS:FuGIMA* and *UAS:FuGIMA-C3PA* transgenic lines, and performed anatomical registrations and complementation analyses. Y.W. performed the imaging on RGC terminal responses and analyzed the direction-selective responses in RGCs. F.K. generated the *UAS:syGCaMP6s* transgenic line. A.K., Y.W., and F.K. annotated arborization fields. A.K., Y.W., H.B., and F.K. wrote the manuscript.

DECLARATION OF INTERESTS

The authors declare no competing interests.

Received: December 21, 2018
Revised: February 17, 2019
Accepted: April 10, 2019
Published: May 27, 2019

REFERENCES

Ahrens, M.B., Orger, M.B., Robson, D.N., Li, J.M., and Keller, P.J. (2013). Whole-brain functional imaging at cellular resolution using light-sheet microscopy. Nat. Methods *10*, 413–420.

Arrenberg, A.B., Del Bene, F., and Baier, H. (2009). Optical control of zebrafish behavior with halorhodopsin. Proc. Natl. Acad. Sci. USA *106*, 17968–17973.

Avants, B.B., Epstein, C.L., Grossman, M., and Gee, J.C. (2008). Symmetric diffeomorphic image registration with cross-correlation: evaluating automated labeling of elderly and neurodegenerative brain. Med. Image Anal. *12*, 26–41.

Avants, B.B., Yushkevich, P., Pluta, J., Minkoff, D., Korczykowski, M., Detre, J., and Gee, J.C. (2010). The optimal template effect in hippocampus studies of diseased populations. Neuroimage *49*, 2457–2466.

Avants, B.B., Tustison, N.J., Song, G., Cook, P.A., Klein, A., and Gee, J.C. (2011). A reproducible evaluation of ANTs similarity metric performance in brain image registration. Neuroimage *54*, 2033–2044.

Baier, H. (2000). Zebrafish on the move: towards a behavior-genetic analysis of vertebrate vision. Curr. Opin. Neurobiol. *10*, 451–455.

Barlow, H.B., and Hill, R.M. (1963). Selective sensitivity to direction of movement in ganglion cells of the rabbit retina. Science *139*, 412–414.

Biot, E., Crowell, E., Höfte, H., Maurin, Y., Vernhettes, S., and Andrey, P. (2008). A new filter for spot extraction in N-dimensional biological imaging. In Fifth IEEE International Symposium on Biomedical Imaging (ISBI'08) (From Nano to Macro (IEEE)), pp. 975–978.

Burrill, J.D., and Easter, S.S., Jr. (1994). Development of the retinofugal projections in the embryonic and larval zebrafish (Brachydanio rerio). J. Comp. Neurol. *346*, 583–600.

Cazin, L., Precht, W., and Lannou, J. (1980). Pathways mediating optokinetic responses of vestibular nucleus neurons in the rat. Pflugers Arch. *384*, 19–29.

Chen, X., Mu, Y., Hu, Y., Kuan, A.T., Nikitchenko, M., Randlett, O., Chen, A.B., Gavornik, J.P., Sompolinsky, H., Engert, F., and Ahrens, M.B. (2018). Brainwide organization of neuronal activity and convergent sensorimotor transformations in larval zebrafish. Neuron *100*, 876–890.e5.

Dal Maschio, M., Donovan, J.C., Helmbrecht, T.O., and Baier, H. (2017). Linking neurons to network function and behavior by two-photon holographic optogenetics and volumetric imaging. Neuron *94*, 774–789.e5.

Del Bene, F., Wyart, C., Robles, E., Tran, A., Looger, L., Scott, E.K., Isacoff, E.Y., and Baier, H. (2010). Filtering of visual information in the tectum by an identified neural circuit. Science *330*, 669–673.

Dhande, O.S., and Huberman, A.D. (2014). Retinal ganglion cell maps in the brain: implications for visual processing. Curr. Opin. Neurobiol. *24*, 133–142.

Distel, M., Hocking, J.C., Volkmann, K., and Köster, R.W. (2010). The centrosome neither persistently leads migration nor determines the site of axonogenesis in migrating neurons in vivo. J. Cell Biol. *191*, 875–890.

Dreosti, E., Odermatt, B., Dorostkar, M.M., and Lagnado, L. (2009). A genetically encoded reporter of synaptic activity in vivo. Nat. Methods *6*, 883–889.

Dunn, T.W., Gebhardt, C., Naumann, E.A., Riegler, C., Ahrens, M.B., Engert, F., and Del Bene, F. (2016). Neural circuits underlying visually evoked escapes in larval zebrafish. Neuron *89*, 613–628.

Feng, L., Zhao, T., and Kim, J. (2015). neuTube 1.0: a new design for efficient neuron reconstruction software based on the SWC format. eNeuro *2*, ENEURO.0049-14.2014.

Förster, D., Kramer, A., Baier, H., and Kubo, F. (2018). Optogenetic precision toolkit to reveal form, function and connectivity of single neurons. Methods *150*, 42–48.

Freeman, J., Vladimirov, N., Kawashima, T., Mu, Y., Sofroniew, N.J., Bennett, D.V., Rosen, J., Yang, C.T., Looger, L.L., and Ahrens, M.B. (2014). Mapping brain activity at scale with cluster computing. Nat. Methods *11*, 941–950.

Fujimoto, E., Gaynes, B., Brimley, C.J., Chien, C.B., and Bonkowsky, J.L. (2011). Gal80 intersectional regulation of cell-type specific expression in vertebrates. Dev. Dyn. *240*, 2324–2334.

Gabriel, J.P., Trivedi, C.A., Maurer, C.M., Ryu, S., and Bollmann, J.H. (2012). Layer-specific targeting of direction-selective neurons in the zebrafish optic tectum. Neuron *76*, 1147–1160.

Gebhardt, C., Baier, H., and Del Bene, F. (2013). Direction selectivity in the visual system of the zebrafish larva. Front. Neural Circuits *7*, 111.

Giovannucci, A., Friedrich, J., Gunn, P., Kalfon, J., Brown, B.L., Koay, S.A., Taxidis, J., Najafi, F., Gauthier, J.L., Zhou, P., et al. (2019). CaImAn: an open source tool for scalable calcium imaging data analysis. eLife *8*, e38173.

Heap, L.A., Goh, C.C., Kassahn, K.S., and Scott, E.K. (2013). Cerebellar output in zebrafish: an analysis of spatial patterns and topography in eurydendroid cell projections. Front. Neural Circuits *7*, 53.

Helmbrecht, T.O., dal Maschio, M., Donovan, J.C., Koutsouli, S., and Baier, H. (2018). Topography of a visuomotor transformation. Neuron *100*, 1429–1445.e4.

Jefferis, G.S.X.E., and Manton, J.D. (2014). NeuroAnatomy Toolbox v1.5.2 (ZENODO).

Kaifosh, P., Zaremba, J.D., Danielson, N.B., and Losonczy, A. (2014). SIMA: Python software for analysis of dynamic fluorescence imaging data. Front. Neuroinform. *8*, 80.

Knogler, L.D., Markov, D.A., Dragomir, E.I., Štih, V., and Portugues, R. (2017). Sensorimotor representations in cerebellar granule cells in larval zebrafish are dense, spatially organized, and non-temporally patterned. Curr. Biol. *27*, 1288–1302.

Kubo, F., Hablitzel, B., Dal Maschio, M., Driever, W., Baier, H., and Arrenberg, A.B. (2014). Functional architecture of an optic flow-responsive area that drives horizontal eye movements in zebrafish. Neuron *81*, 1344–1359.

Kunst, M., Laurell, E., Mokayes, N., Kramer, A., Kubo, F., Fernandes, A.M., Förster, D., Dal Maschio, M., and Baier, H. (2019). A cellular-resolution atlas of the larval zebrafish brain. Neuron *103*, this issue, 21–38.

Longair, M., and Jefferis, G.S. (2006). Name landmarks and register. Fiji plugin. https://imagej.net/name_landmarks_and_register.

Longair, M.H., Baker, D.A., and Armstrong, J.D. (2011). Simple Neurite Tracer: open source software for reconstruction, visualization and analysis of neuronal processes. Bioinformatics *27*, 2453–2454.

Lowe, A.S., Nikolaou, N., Hunter, P.R., Thompson, I.D., and Meyer, M.P. (2013). A systems-based dissection of retinal inputs to the zebrafish tectum reveals different rules for different functional classes during development. J. Neurosci. *33*, 13946–13956.

Marquart, G.D., Tabor, K.M., Horstick, E.J., Brown, M., Geoca, A.K., Polys, N.F., Nogare, D.D., and Burgess, H.A. (2017). High-precision registration between zebrafish brain atlases using symmetric diffeomorphic normalization. Gigascience *6*, 1–15.

Masseck, O.A., and Hoffmann, K.P. (2009a). Comparative neurobiology of the optokinetic reflex. Ann. N Y Acad. Sci. *1164*, 430–439.

Masseck, O.A., and Hoffmann, K.P. (2009b). Question of reference frames: visual direction-selective neurons in the accessory optic system of goldfish. J. Neurophysiol. *102*, 2781–2789.

Matsui, H., Namikawa, K., Babaryka, A., and Köster, R.W. (2014). Functional regionalization of the teleost cerebellum analyzed in vivo. Proc. Natl. Acad. Sci. USA *111*, 11846–11851.

Mazurek, M., Kager, M., and Van Hooser, S.D. (2014). Robust quantification of orientation selectivity and direction selectivity. Front. Neural Circuits *8*, 92.

Meyer, M.P., and Smith, S.J. (2006). Evidence from in vivo imaging that synaptogenesis guides the growth and branching of axonal arbors by two distinct mechanisms. J. Neurosci. *26*, 3604–3614.

Naumann, E.A., Fitzgerald, J.E., Dunn, T.W., Rihel, J., Sompolinsky, H., and Engert, F. (2016). From whole-brain data to functional circuit models: the zebrafish optomotor response. Cell *167*, 947–960.e20.

Neuhauss, S.C., Biehlmaier, O., Seeliger, M.W., Das, T., Kohler, K., Harris, W.A., and Baier, H. (1999). Genetic disorders of vision revealed by a behavioral screen of 400 essential loci in zebrafish. J. Neurosci. *19*, 8603–8615.

Nikolaou, N., Lowe, A.S., Walker, A.S., Abbas, F., Hunter, P.R., Thompson, I.D., and Meyer, M.P. (2012). Parametric functional maps of visual inputs to the tectum. Neuron *76*, 317–324.

Orger, M.B., Smear, M.C., Anstis, S.M., and Baier, H. (2000). Perception of Fourier and non-Fourier motion by larval zebrafish. Nat. Neurosci. *3*, 1128–1133.

Orger, M.B., Gahtan, E., Muto, A., Page-McCaw, P., Smear, M.C., and Baier, H. (2004). Behavioral screening assays in zebrafish. Methods Cell Biol. *77*, 53–68.

Orger, M.B., Kampff, A.R., Severi, K.E., Bollmann, J.H., and Engert, F. (2008). Control of visually guided behavior by distinct populations of spinal projection neurons. Nat. Neurosci. *11*, 327–333.

Paquet, D., Bhat, R., Sydow, A., Mandelkow, E.M., Berg, S., Hellberg, S., Fälting, J., Distel, M., Köster, R.W., Schmid, B., and Haass, C. (2009). A zebrafish model of tauopathy allows in vivo imaging of neuronal cell death and drug evaluation. J. Clin. Invest. *119*, 1382–1395.

Patterson, G.H., and Lippincott-Schwartz, J. (2002). A photoactivatable GFP for selective photolabeling of proteins and cells. Science *297*, 1873–1877.

Pittman, A.J., Law, M.Y., and Chien, C.B. (2008). Pathfinding in a large vertebrate axon tract: isotypic interactions guide retinotectal axons at multiple choice points. Development *135*, 2865–2871.

Pnevmatikakis, E.A., and Giovannucci, A. (2017). NoRMCorre: an online algorithm for piecewise rigid motion correction of calcium imaging data. J. Neurosci. Methods *291*, 83–94.

Pologruto, T.A., Sabatini, B.L., and Svoboda, K. (2003). ScanImage: flexible software for operating laser scanning microscopes. Biomed. Eng. Online *2*, 13.

Portugues, R., and Engert, F. (2009). The neural basis of visual behaviors in the larval zebrafish. Curr. Opin. Neurobiol. *19*, 644–647.

Portugues, R., Feierstein, C.E., Engert, F., and Orger, M.B. (2014). Whole-brain activity maps reveal stereotyped, distributed networks for visuomotor behavior. Neuron *81*, 1328–1343.

Rinner, O., Rick, J.M., and Neuhauss, S.C. (2005). Contrast sensitivity, spatial and temporal tuning of the larval zebrafish optokinetic response. Invest. Ophthalmol. Vis. Sci. *46*, 137–142.

Robles, E., Laurell, E., and Baier, H. (2014). The retinal projectome reveals brain-area-specific visual representations generated by ganglion cell diversity. Curr. Biol. *24*, 2085–2096.

Ruta, V., Datta, S.R., Vasconcelos, M.L., Freeland, J., Looger, L.L., and Axel, R. (2010). A dimorphic pheromone circuit in Drosophila from sensory input to descending output. Nature *468*, 686–690.

Sabbah, S., Gemmer, J.A., Bhatia-Lin, A., Manoff, G., Castro, G., Siegel, J.K., Jeffery, N., and Berson, D.M. (2017). A retinal code for motion along the gravitational and body axes. Nature *546*, 492–497.

Schiff, D., Cohen, B., and Raphan, T. (1988). Nystagmus induced by stimulation of the nucleus of the optic tract in the monkey. Exp. Brain Res. *70*, 1–14.

Schindelin, J., Arganda-Carreras, I., Frise, E., Kaynig, V., Longair, M., Pietzsch, T., Preibisch, S., Rueden, C., Saalfeld, S., Schmid, B., et al. (2012). Fiji: an open-source platform for biological-image analysis. Nat. Methods *9*, 676–682.

Schneider, C.A., Rasband, W.S., and Eliceiri, K.W. (2012). NIH Image to ImageJ: 25 years of image analysis. Nat. Methods *9*, 671–675.

Scott, E.K., Mason, L., Arrenberg, A.B., Ziv, L., Gosse, N.J., Xiao, T., Chi, N.C., Asakawa, K., Kawakami, K., and Baier, H. (2007). Targeting neural circuitry in zebrafish using GAL4 enhancer trapping. Nat. Methods *4*, 323–326.

Semmelhack, J.L., Donovan, J.C., Thiele, T.R., Kuehn, E., Laurell, E., and Baier, H. (2014). A dedicated visual pathway for prey detection in larval zebrafish. eLife *3*, e04878.

Stuermer, C.A. (1988). Retinotopic organization of the developing retinotectal projection in the zebrafish embryo. J. Neurosci. *8*, 4513–4530.

Temizer, I., Donovan, J.C., Baier, H., and Semmelhack, J.L. (2015). A visual pathway for looming-evoked escape in larval zebrafish. Curr. Biol. *25*, 1823–1834.

Vishwanathan, A., Daie, K., Ramirez, A.D., Lichtman, J.W., Aksay, E.R.F., and Seung, H.S. (2017). Electron microscopic reconstruction of functionally identified cells in a neural integrator. Curr. Biol. *27*, 2137–2147.e3.

Vladimirov, N., Wang, C., Höckendorf, B., Pujala, A., Tanimoto, M., Mu, Y., Yang, C.T., Wittenbach, J.D., Freeman, J., Preibisch, S., et al. (2018). Brain-wide circuit interrogation at the cellular level guided by online analysis of neuronal function. Nat. Methods *15*, 1117–1125.

Wang, K., Hinz, J., Haikala, V., Reiff, D.F., and Arrenberg, A.B. (2019). Selective processing of all rotational and translational optic flow directions in the zebrafish pretectum and tectum. BMC Biol. *17*, 29.

Westerfield, M. (2007). The Zebrafish Book. A Guide for the Laboratory Use of Zebrafish (Danio rerio), Fifth Edition (Eugene: Univ. of Oregon Press).

Wylie, D.R., Bischof, W.F., and Frost, B.J. (1998). Common reference frame for neural coding of translational and rotational optic flow. Nature *392*, 278–282.

Yáñez, J., Suárez, T., Quelle, A., Folgueira, M., and Anadón, R. (2018). Neural connections of the pretectum in zebrafish (Danio rerio). J. Comp. Neurol. *526*, 1017–1040.

Zhang, B.B., Yao, Y.Y., Zhang, H.F., Kawakami, K., and Du, J.L. (2017). Left habenula mediates light-preference behavior in zebrafish via an asymmetrical visual pathway. Neuron *93*, 914–928.e4.

STAR★METHODS

KEY RESOURCES TABLE

REAGENT or RESOURCE	SOURCE	IDENTIFIER
Chemicals, Peptides, and Recombinant Proteins		
Alpha-Bungarotoxin	Invitrogen	B1601
DiI (1,1'-Dioctadecyl-3,3,3′,3′-Tetramethylindocarbocyanine Perchlorate)	Invitrogen	D3911
Tricaine	Sigma-Aldrich	MS-222
Experimental Models: Organisms/Strains		
Zebrafish *Tg(atoh7:Gal4-VP16)s1992t, a. k. a. ath5:Gal4*	Del Bene et al., 2010	ZFIN ID: ZDB-FISH-150901-27082
Zebrafish Tg*(elavl3:lyn-tagRFP)mpn404, a. k. a. HuC:lyn-tagRFP*	Dal Maschio et al., 2017	ZFIN ID: ZDB-ALT-170731-38
Zebrafish *Tg(elavl3:GCaMP5G)a4598*	Ahrens et al., 2013	ZFIN ID: ZDB-FISH-150901-22335
Tg(elavl3:Has.H2B-GCaMP6s)jf5 aka HuC:H2B-GCaMP6s	Freeman et al., 2014	ZFIN ID: ZDB-FISH-170711-1
Zebrafish *Et(E1b:Gal4-VP16)s1101t)*	Scott et al., 2007	ZFIN ID: ZDB-FISH-150901-5255
Zebrafish*Tg(isl2b:Gal4-VP16, myl7:TagRFP)zc65*	Fujimoto et al., 2011	ZFIN ID: ZDB-FISH-150901-13523
Zebrafish *Tg(UAS:mCherry)s1984t*	Heap et al., 2013	ZFIN ID: ZDB-FISH-150901-14417
Zebrafish *Tg(UAS:syn-GFP) a. k. a. UAS:sypGFP*	Heap et al., 2013	ZFIN ID: ZDB-FISH-150901-21811
Zebrafish *Tg(UAS:Dendra-kras)s1998t*	Arrenberg et al., 2009	ZFIN ID: ZDB-ALT-110808-3
Zebrafish *Tg(UAS:syGCaMP6s)mpn156*	This paper	NA
Zebrafish *Tg(UAS-Janus:nlsGCaMP6s,PA-GFP)mpn161, a.k.a. UAS:FuGIMA*	This paper	NA
Zebrafish *Tg(UAS-Janus:nlsGCaMP6s,C3PA-GFP)mpn162, a.k.a UAS:FuGIMA-C3PA*	This paper	NA
Software and Algorithms		
ImageJ/Fiji	Schindelin et al., 2012	https://fiji.sc/
Simple Neurite Tracer (Fiji plugin)	Longair et al., 2011	https://imagej.net/Simple_Neurite_Tracer
Attenuation Correction (Fiji plugin)	Biot et al., 2008	http://imagejdocu.tudor.lu/doku.php?id=plugin:stacks:attenuation_correction:start
Name Landmarks and Register (Fiji plugin)	Longair and Jefferis, 2006	https://imagej.net/Name_Landmarks_and_Register
NeuTube	Feng et al., 2015	https://www.neutracing.com/
Advanced Normalization Tools (ANTs)	Avants et al., 2008; Avants et al., 2011; Avants et al., 2010	http://stnava.github.io/ANTs/
RStudio Version 1.0.143	RStudio	https://www.rstudio.com/
Python 2.7	Python.org	https://www.python.org
Python 3	Python.org	https://www.python.org
Amira	Thermo Fisher Scientific	https://www.thermofisher.com/global/en/home/industrial/electron-microscopy/electron-microscopy-instruments-workflow-solutions/3d-visualization-analysis-software/amira-life-sciences-biomedical.html
Imaris	Bitplane	https://imaris.oxinst.com
FFmpeg		https://ffmpeg.org/
CaImAn (Calcium Imaging Analysis toolbox)	Giovannucci et al., 2019; Pnevmatikakis and Giovannucci, 2017	https://github.com/flatironinstitute/CaImAn
R package nat (NeuroAnatomy Toolbox)	Jefferis and Manton, 2014	http://jefferis.github.io/nat/
R package rgl	Daniel Adler, Duncan Murdoch and others	https://cran.r-project.org/web/packages/rgl/index.html

(*Continued on next page*)

Continued

REAGENT or RESOURCE	SOURCE	IDENTIFIER
Other		
Confocal microscope LSM 700, with a 20x/1.0 NA water-dipping objective	Carl Zeiss	https://www.zeiss.com/microscopy/int/home.html?vaURL=www.zeiss.com/microscopy
Movable object two-photon microscope with a 20x water-dipping objective (Olympus, NA 1.0)	Sutter Instruments/ Olympus	https://www.sutter.com / https://www.olympus-lifescience.com/de/
Femtonics 3DRC two-photon microscope, with 16x or 20x water-dipping objective	Femtonics	http://femtonics.eu/
Tracings, brain area annotations, and standard brain	Single-neuron atlas of Kunst et al., 2019	https://fishatlas.neuro.mpg.de/zebrafishatlas/

CONTACT FOR REAGENT AND RESOURCE SHARING

Further information and requests for resources and reagents should be directed to and will be fulfilled by the Lead Contact, Fumi Kubo (fumikubo@nig.ac.jp).

EXPERIMENTAL MODEL AND SUBJECT DETAILS

Animal care and transgenic zebrafish

Adult and larval zebrafish (*Danio rerio*) were housed and handled according to standard procedures (Westerfield, 2007). Animal experiments were performed according to regulations of the Max Planck Society and the regional government of Upper Bavaria (Regierung von Oberbayern; approved protocols: ROB-55.2Vet-2532.Vet_02-16-31 and 55.2-1-54-2532-101-2012). We used the following previously described transgenic lines: *HuC:GCaMP5G (Tg(elavl3:GCaMP5G)a4598); Tg(isl2b:Gal4-VP16)zc65; Tg(atoh7:Gal4-VP16)s1992t; Tg(UAS:mCherry)s1984t; Tg(UAS:Dendra-kras)s1998t; Tg(UAS:sypGFP); Et(E1b:Gal4-VP16)s1101t (= Gal4^{s1101t}), HuC:lyn-tagRFP (Tg(elavl3:lyn-tagRFP)mpn404); Tg(elavl3:H2B-GCaMP6s).* Transgenic fish were kept in either a TL or TLN (nacre) background and larvae lacking trunk pigmentation (outcrossed to TLN, nacre) were used in the experiment. Zebrafish larvae were raised in Danieau's solution until day 5 or 6 post-fertilization (dpf). As sex determination has not yet taken place in larvae, we used future males and females indiscriminately.

Line establishment

To generate the *UAS:syGCaMP6s* plasmid, the synaptophysin coding sequence (Meyer and Smith, 2006) was fused with GCaMP6s and inserted into a pTol2-14xUAS vector. *Tg(UAS:syGCaMP6s)mpn156* transgenic fish were generated using the standard Tol2 transposon system.

To co-express nls-GCaMP6s and either paGFP (for *UAS:FuGIMA*) or C3PA-GFP (for *UAS:FuGIMA-C3PA*), we fused nls-GCaMP6s and either paGFP (Patterson and Lippincott-Schwartz, 2002) or C3PA-GFP (Ruta et al., 2010) to the two sides of a bidirectional 14x UAS sequence (Janus-UAS; Distel et al., 2010; Paquet et al., 2009) in a Tol2 vector harboring a trangenesis marker ("bleeding heart," *cmlc2:mCherry*). The transgenic lines *Tg(UAS:paGFP,nlsGCaMP6s)mpn161* and *Tg(UAS:C3PA-GFP,nlsGCaMP6s)mpn162* were generated in the background of *Gal4^{s1101t}* using the standard Tol2 transposon system. Most FuGIMA experiments were conducted in the F2 and F3 generations of the *UAS:FuGIMA* line, which showed considerable variegation and silencing of the transgene expression. Of the 58 FuGIMA tracings, three were performed with *UAS:FuGIMA-C3PA, Gal4^{s1101t}* or *HuC:Gal4.* These neurons belong to the monocular direction-selective response type class and do not intersect with AF5.

METHOD DETAILS

RGC axons and pretectal neuropil functional imaging

Calcium imaging of RGC terminals was performed in triple transgenic zebrafish larvae expressing syGCaMP6s and mCherry in RGCs (*Tg(isl2b:Gal4-VP16)zc65, Tg(UAS:syGCaMP6s)mpn156, Tg(UAS:mCherry)s1984t*) between 5 and 6 dpf. Larvae were mounted in 2% low-melting agarose with the dorsal side up. The fish were positioned in the center of a dish with a diameter of 3 cm. Larvae were intraspinally injected with α-bungarotoxin (2 mg/mL α-bungarotoxin (Invitrogen, B1601), FastRed 10% v/v, 1x Danieau's solution). A moveable objective microscope (MOM, Sutter Instruments) was used to record GCaMP signals (920 nm, 10-20 mW after the objective) with a 20x objective (Olympus, NA 1.0). ScanImage software (Pologruto et al., 2003) was used for image acquisition. We typically recorded one of two volumes per fish, each covering AF10 or AF4, AF5 and AF6 volume. For recording of AF10, ca. 20 z-planes were imaged with the z-step size of 4 μm. For recording of AF4, 5 and 6, ca. 25 z-planes were imaged with the z-step size of 3 μm. For each z-plane, images were acquired with a spatial resolution of 256x256 pixels (pixel size of 0.33 μm for AF10 and 0.19 μm for AF 4, 5 and 6) at a frame rate of 2.38 Hz. Since the average diameter of a presynaptic bouton in zebrafish RGCs

is ~0.8 μm (Meyer and Smith, 2006), the physical lateral dimensions of pixels are below that of a typical presynaptic bouton. Sinusoidal grating stimuli were generated by custom written scripts using PsychoPy and presented onto a screen positioned either below or on the side of the fish using a digital light processing (DLP) projector (DLP LightCrafter 4500), using the red channel only, which allowed simultaneous visual stimulation and detection of green fluorescence. The visual stimuli consisted of whole-field luminance change (lowest luminance → highest luminance → lowest luminance) followed by gratings moving in 12 equally spaced angular directions presented in a random order. For each presentation of a different direction, the gratings initially stayed stationary for 10 s, in motion for 5 s, and back to stationary for 5 s, and this process was repeated for all grating presentations. The total length of the visual stimulus protocol was about 5 min. For the projection from the side of the fish, spatial and temporal frequency of the gratings was 0.06 cycle/degree and 1.8 Hz, respectively. The projected image filled a visual field of approximately 120° in azimuth and ± 35° in elevation. For the projection from below the fish, gratings were designed as described in the recent study (Naumann et al., 2016). Briefly, the gratings of the spatial period of 1 cm moving at 10 mm/sec were presented onto a 12 cm x 12 cm screen. In contrast to this recent study, the complete screen area was covered by the grating (no stimulus omission directly below the fish).

Calcium imaging of pretectal neuropil was performed in *HuC:GCaMP5G* fish between 5 and 6 dpf. A volume centered around the pretectal neuropil was imaged with the z-step size of 5 μm. For each z-plane, images were acquired with a spatial resolution of 512x512 pixels (pixel size of 0.19 μm) at a frame rate of 2.38 Hz. The visual stimulus was presented from below the fish, as described above.

Pixelwise calcium imaging analysis (RGCs)

Raw time series of two-photon recordings were first corrected for motion artifacts by a hidden Markov model (HMM)-based algorithm using the SIMA toolkit (Kaifosh et al., 2014) and then processed by a uniform filter for noise removal. For each pixel in the filtered motion corrected recordings, its fluorescence time series was divided into 14 phases based on the visual stimuli. These 14 phases consisted of 1 ON phase (whole-field luminance increase), 1 OFF phase (whole-filed luminance decrease), and 12 motion phases. The normalized signal intensity changes ($\Delta F/F_0$) were calculated for each phase, and they were tested for correlation with the stimulus time series convolved with a kernel with syGGCaMP6s kinetics (τ_{decay} = 1.2 s). Pixels were considered motion responsive, if 1) their Pearson correlation coefficients were above the threshold of 0.35 in no less than 2 motion phases and 2) their t-scores (the coefficient from linear regression divided by error) in at least one motion phase were above noise threshold of 1.3. For each motion responsive pixel, we generated a response profile which consisted of the integral response over motion presentation for 12 directions.

To identify DS and OS populations, we plotted the response profiles as vectors in direction and orientation space, and we calculated the vector sum. The angle of the vector sum represents the preferred direction or orientation, and the normalized length of the vector sum (L_{dir} and L_{ori} as calculated below) represents the degree of selectivity. This has been shown to be a robust method to quantify direction and orientation selectivity (Mazurek et al., 2014).

$$L_{dir} = \left| \frac{\sum_k R(\theta_k)\exp(i\theta_k)}{\sum_k R(\theta_k)} \right|$$

$$L_{ori} = \left| \frac{\sum_k R(\theta_k)\exp(2i\theta_k)}{\sum_k R(\theta_k)} \right|$$

θk represents a direction of motion, and $R(\theta k)$ is the integral response during the motion phase in the direction of θk. An empirical threshold of 0.4 was set for L_{ori} and 0.5 for L_{dir}. Pixels that surpassed the threshold were considered DS or OS. If a pixel was classified as both DS and OS, that pixel was regarded as DS, for which we have set a more stringent threshold. This ensured that DS and OS pixels are mutually exclusive. These thresholded, binary DS and OS pixels were color coded according to their preferred direction or orientation and plotted on top of the anatomical references, which are the mean images of the motion-corrected time series. To generate histograms of preferred direction (Figure 4), we first obtained the distribution of the preferred direction of DS pixels for each individual fish. The total number of DS pixels was normalized across different fish, and then the average of the normalized distribution was plotted. To compare our data with the previously published result of distribution of preferred directions of DS-RGC terminals (Figure 4D), we selected 3 planes (separated by 4 μm) in the dorsal part of AF10 (approximately 30 - 45 μm from the dorsal surface of the tectum). The luminance response was determined independently of the response to motion stimuli (Figure S6). Pixels were deemed luminance responsive, if they showed activity correlated with changes in light intensity (Pearson correlation coefficient > empirically derived threshold 0.45). The activity of ON pixels increases when luminance rises, while that of OFF pixels increases when luminance drops. ON-OFF pixels show an increase in activity when luminance rises and drops. For a pixel to be regarded as luminance responsive, mutually exclusive criteria were used: i.e., ON if ON > 0.45 and OFF < 0.45, and OFF if ON < 0.45 and OFF > 0.45, and ON-OFF if ON > 0.45 and OFF > 0.45.

Image registration for RGC and pretectal neuropil

After calcium imaging, we acquired anatomical z stacks of the same fish (*isl2b:Gal4, UAS:syGCaMP6s, UAS:mCherry*). We first obtained small stacks (256x256 pixels) with the two-photon microscope, using syGCaMP6s and covering the functionally imaged

volume (either AF10 or AF4, AF5 and AF6, or both in a few cases). Additionally, one overview stack with a higher resolution (1024x1024 pixels) was taken at the confocal microscope (LSM700, Carl Zeiss, Jena, Germany) with a 20x objective (W Plan-Apochromat 20x/1.0, Carl Zeiss, NA 1.0) with a z-step size of 1 μm and using both syGCaMP6s and mCherry channels.

In order to visualize the DS and OS RGC terminals imaged in multiple fish and compare them with the *HuC:GCaMP5G* expression pattern, we developed a three-step registration procedure (Figure S5A): 1) the mean image of the motion corrected time series were manually aligned (custom written Python script) onto the two-photon anatomical z stack using the syGCaMP6s signal as reference. As such, we registered the functional information to the anatomical z stacks. To circumvent changes of pixel values and thereby changes of DS/OS information caused by the image registration, we binned functional data according to preferred direction/orientation. Namely, we created 12 separate channels, with each channel corresponding to one of the 12 bins of preferred directions. 2) the two-photon anatomical z stacks were registered to the confocal stack of the same fish using syGCaMP6s as the reference channel. To facilitate gross alignment between the stacks, we pre-aligned the z stacks according to manual landmark selection using the plugin "Name Landmarks and Register" (by Mark Longair and Greg Jefferis) in Fiji (Schindelin et al., 2012; Schneider et al., 2012). The stacks were then precisely registered by the image registration library ANTs (Advanced Normalization Tools) (Avants et al., 2008; Avants et al., 2011; Avants et al., 2010) using syGCaMP6s signal as a reference for registration. The parameters for the command antsRegistration recently applied to zebrafish live images (Marquart et al., 2017) were used, except for variation of the initial transform parameter and the application of a mask. This mask was drawn in Fiji with the plugin segmentation editor (by Johannes Schindelin, Francois Kusztos and Benjamin Schmid) and restricted the search for corresponding pixels to the area containing RGC terminals. 3) The resulting stack was then registered to the template (RGC standard brain) which was generated from six different stacks *(isl2b:Gal4, UAS:mCherry)* using the command antsMultivariateTemplateConstruction2 in ANTs. Using the mCherry signal as a reference channel, we applied the same settings as for the previous round of ANTs registration (but without mask). Therefore, for each step of registration, the previous template stack served as the pattern to be registered. If a pitch difference between the experimental fish and the template was greater than ± 5° (as calculated from the transformation information), DS and OS bins were recalculated accordingly before applying image registration. After anatomical stacks underwent registration, functional stacks containing DS/OS information were treated as additional channels and subjected to the same transformations using the command antsApplyTransforms (Marquart et al., 2017). As DS/OS depicting pixels were broadened due to registration, we applied a threshold of a pixel intensity value 50 to eliminate the smearing effect of the registration (custom Python script). This threshold was determined visually to display the same spatial extent of DS/OS information in the template volume as in the original two-photon frames. To visualize the isl2b template in the context of the *HuC:GCaMP5G* expression pattern, we registered a single *isl2b:Gal4, UAS:mCherry, HuC:GCaMP5G* fish to the template via the mCherry channel. For registering DS neuropil signals imaged in *HuC:GCaMP5G* fish (N = 6 fish), the same image registration protocol was applied except that 1) pre-alignment of the two-photon anatomical z stacks using manual landmark selection was skipped (during step 2 of the registration protocol) and 2) the confocal anatomical stacks of the functionally imaged fish were registered to our reference brain via the previously aligned *HuC:GCaMP5G* pattern.

Segmentation of AFs and 3D rendering

Segmentation of AFs was performed based on presynaptic puncta signals in *atoh7:Gal4, UAS:sypGFP* fish after they had been registered to the RGC standard brain using ANTs. AFs were manually segmented using published anatomical information about AFs (Burrill and Easter, 1994; Robles et al., 2014). Note that our segmentation of AFs relied only on anatomical features, without referring to functional maps of RGC terminals. We noted some variability of SypGFP localization patterns across different individual fish, especially at the boundary between AF5 and AF6. To account for this individual fish differences, 3 fish were segmented by 3 annotators each, and average of the 9 annotations was used to generate a consensus mask for AF4, AF5 and AF6. To quantify the number of DS pixels in different AFs, we used original calcium time series before anatomical registration to avoid the smearing effect (thereby leading to changes in the absolute number of pixels of each RGC puncta) caused by the registration. To count DS pixels in the original calcium time series in each AF, we either drew masks of AFs directly on the original calcium time series (with the aid of anatomical stacks) or back-transformed our consensus AF masks (drawn on the registered image volume) to the original calcium time series using inverse transformation. To determine the proportion of DS pixels relative to the entire number of pixels in AFs, we first quantified the pixel counts in AF5 and AF6 using the synaptic puncta signals of 9 anatomical stacks obtained from *isl2b:Gal4, UAS:sypGFP* fish. Subsequently, the number of DS pixels was divided by the average pixel counts in each AF to derive the percentage of DS pixels per total number of pixels in each AF. 3D rendering of registered image stacks was performed using Imaris software. Autofluorescence of the skin and eyes was removed by applying 3D masks and the volumes corresponding to AFs were highlighted in Imaris. Movies were prepared using Imaris and Fiji.

Lipophilic Dye labeling

6 day old *isl2b:Gal4, UAS:Dendra-kras* transgenic larvae were fixed in 4% paraformaldehyde in PBS for 1hr at 4°C. 1% solutions of DiI in chloroform were pressure injected between the lens and the retina to visualize all axonal projections. Fluorescent images were acquired one day after the injection.

Functional imaging and analysis (FuGIMA dataset)

Larvae were mounted in agarose (LMP-agarose, 1.5% w/v in Danieau's solution), and intraspinally injected with alpha-bungarotoxin (2 mg/mL α-bungarotoxin (Invitrogen, B1601), FastRed 10% v/v, 1x Danieau's solution) before the experiment to abolish movements. During injection, larvae were under anesthesia with tricaine (0,02%, MS-222, Sigma-Aldrich) and the tricaine was washed out after injection. We used a two-photon microscope (Femtonics 3DRC microscope, Femtonics, Tuzlo, Hungary) for functional imaging as well as acquisition of z stacks. The visual stimuli were presented to the fish using a custom-built red LED arena as reported previously (Kubo et al., 2014; four flat panels covering 360° around the fish; no grating presentation in ~30° in front of the fish). In each experiment session, gratings moved horizontally in eight phases (3 s each at spatial frequency of 0.033 cycles/degree and temporal frequency of 2 cycles/sec, interspersed with 10 s stationary gratings, Figure S2A). Four of the eight phases are monocular, four are binocular: 1) left nasalward, 2) left temporalward, 3) right temporalward, 4) right nasalward, 5) backward, 6) forward, 7) clockwise, 8) counterclockwise. The sequence of eight phases was repeated three times. During visual stimulation, GCaMP fluorescence was imaged at about 3 Hz using the laser tuned to 920 nm (0.5 × 0.5 μm/pixel, ca. 15 mW after the objective, imaging region of about 90 × 98 μm). Response types of recorded neurons were identified using a custom written python script (regressor based, near-online analysis: approx. 2 minutes run time). First, traces of the three repetitions were averaged. Second, the averaged time series of each pixel were correlated to 256 regressors (visual stimulus time series convolved with nls-GCaMP6s kernel, tau = 3 s, tau determined visually to resemble the fluorescence trace), and the best-correlated regressor was determined for each pixel (threshold of Pearson's correlation coefficient > 0.3). For each regressor-of-interest (e.g., monocular DS and translation-selective response types), we generated a map of correlated pixels overlaid on the mean $\Delta F/F_0$ image (Figure 1E), based on which cells of interest were chosen. The selected cells of interest were further manually inspected for variability in response across repetitions, baseline fluorescence (indicator of transgene expression level), and accessibility for photoactivation (separation from neighboring neurons).

To improve display of fluorescence traces, functional imaging time series were motion corrected with CaImAn (Giovannucci et al., 2019; Pnevmatikakis and Giovannucci, 2017). We extracted average brightness from ROIs centered on the cell of interest (using Fiji), and calculated $\Delta F/F_0$ with F_0 being the mean of the 10^{th} percentile. For neurons of the monocular DS and translation selective type, we plotted the mean trace of three repetitions, grouped by response type. For non-motion-selective neurons we in addition plotted the variance over three stimulus repetitions of the trial (SEM). Regressor traces were manually overlaid with corresponding fluorescence traces.

Photoactivation of paGFP and z stack acquisition

Photoactivation of paGFP in selected cells of interest was performed according to a detailed published protocol (Förster et al., 2018). Briefly, a ROI of about 0.8 × 0.8 μm (0.2 × 0.2 μm/pixel, 4 × 4 pixels) was placed in the center of the nucleus in 3D. Initially, paGFP was photoactivated with trial pulses of 200 ms (one and three pulses, laser wavelength 750 nm, ca. 10 - 17 mW after the objective, 1 Hz). If no neighboring cells were photoactivated, the ROI was re-centered and the first full cycle of photoactivation was delivered (40 × 200 ms, 1 Hz, Figure 1F). In cases of residual movement of the fish, tricaine was added before photoactivation. The whole protocol consisted of 15 cycles, with typically five minutes intervals between two activation cycles. However, in the dataset containing 58 neurons, 3 were photoactivated with less than 5 cycles and 11 with 5-10 cycles of photoactivation. Typically, paGFP fluorescence intensity in the photoactivated soma rapidly increased with the first photoactivation cycle, reaching the maximum after several cycles of photoactivation, suggesting that the maximum level of the photoactivation is achieved after several cycles of photoactivation (Figure S1C). To control progress of diffusion, z stacks capturing both green and red fluorescence (1020 nm, 1 μm z-step) were typically acquired every five cycles, as well as a high resolution stack after the last activation period.

We quantified the degree of photoactivation by calculating the normalized fluorescence change after each cycle of photoactivation (mean of n = 5 neurons in 3 fish). An experiment was terminated, if 1) a directly neighboring neuron was also photoactivated, 2) fluorescence in the neurite did not strongly increase after the first cycle of photoactivation, or 3) the sample drifted. Furthermore, as the pretectum is located directly ventral to the tectum, we photoactivated few neurons resembling tectal neurons' morphology (neurite targeting the tectal neuropil, perpendicular branching in the neuropil layers), which were excluded. Two-photon and confocal microscopy offer different advantages: while two-photon microscopy achieves superior resolution in deeper tissue, it typically does not allow to image close to the eye pigment epithelium (due to photomultiplier tube (PMT) saturation). As confocal microscopy does not show this restriction, we acquired a large z stack at the confocal microscope (LSM 700, Carl Zeiss, Jena, Germany 20x/1.0 NA, water-dipping objective) in addition to the two-photon z stack.

To exclude the possibility that tracing quality underlies differential neurite trajectories of different response types, we manually sorted z stacks into four groups according to their image quality and compared tracings between groups. We did not find systematic differences in tracing length or overall morphology among the four groups (Figure S4C). Furthermore, all four groups contained tracings of all three response classes. Translation-selective neurons were even slightly overrepresented in the "best" image group. It is thus unlikely that we overlooked particular features, such as AF5 targeting, of translation-selective neurons.

Tracing of FuGIMA neurons and consolidation

Neurons were semi-manually traced from the confocal and two-photon z stacks using the Fiji plugin Simple Neurite Tracer (Longair et al., 2011) or the software neuTube (Feng et al., 2015) (Figure 1G). Neurons were traced in both confocal and two-photon z stacks, if available, as the two imaging modalities complement one another (see above). Finally, we merged the tracings of the same neuron

after co-registration (see section Image registration of FuGIMA data below) using a custom written python code. For merging, node locations of two tracings were compared and corresponding nodes were identified based on a maximal distance between them (defined by an empirically chosen tolerance factor). Residual nodes were then added to the merged tracing (OR operation). To assess the labeling distance of paGFP, we photoactivated a neuron co-expressing a membrane-tagged red fluorescent protein and FuGIMA. Briefly, we injected the plasmid *pTol2-UAS:tdTomato-CAAX* into embryos (*Gal4*^{s1101t}*, UAS:FuGIMA*) at the two to four cell stage and selected larvae with sparse expression of tdTomato. We applied the full photoactivation protocol on a spinal cord neuron co-expressing FuGIMA and tdTomato-CAAX. While tdTomato in the soma was considerably photo-bleached, it colocalized with paGFP in the neurite. Neurons highlighted with paGFP can be followed over 200 μm, as shown in a spinal cord neuron co-expressing tdTomato-CAAX (Figures S1A and S1B).

Image registration of FuGIMA data

The basis of comparisons across fish is their registration to a standard brain. We established the FuGIMA standard brain using the ANTs from four z stacks of four live fish expressing *HuC:lyn-tagRFP, HuC:H2B-GCaMP6s* (imaged at the confocal microscope). The FuGIMA standard brain is centered on the pretectum of the right hemisphere and extends 311.2 × 311.2 × 161 μm (x/y/z direction, 0.69 × 0.69 × 1 μm voxel size). To compare tracings from different experimental fish in one volume, z stacks were registered to the standard brain (overlay of three registered example z stacks: Figure 1H, registration workflow: Figure S1D). As preparation, the *HuC:lyn-tagRFP* channel was corrected for depth-dependent decrease of brightness (Fiji plugin Attenuation Correction (Biot et al., 2008)). If the experimental z stack was centered on the contralateral hemisphere, the z stack was flipped and rotated prior to registration using Fiji. Z stacks were registered to the standard brain using the software ANTs (Avants et al., 2008; Avants et al., 2011; Avants et al., 2010) and based on the common reference labeling pattern of *HuC:lyn-tagRFP*. We used the parameters recently determined for live samples (Marquart et al., 2017). Tracings (.swc files) were co-registered using the command ANTsApplyTransformsToPoints contained in the package ANTsR using R. If both confocal and two-photon-stacks were available, two-photon-stacks were registered to the confocal stack of the same fish and confocal stacks were registered to the FuGIMA standard brain. In the case of insufficient registration precision (visually determined), we either altered parameter r to change search initialization or applied a mask to restrict the search area. Search masks (binary .tiff files) were drawn manually or derived from previous rounds of registration. To verify the accuracy of our registration, we annotated eleven anatomical landmarks in the standard brain and individual z stacks (n = 8 z stacks from 6 fish for LM 1 – 9 and 11, n = 6 z stacks from 4 fish for LM 10). After co-registration into the standard brain, we calculated the distance between the landmark of the standard brain and the individual brains using R. The deviations of the landmark positions of the registered fish from those of the standard brain were on average 6.7 ± 2.8 μm (STD, 11 landmarks, 4 or 6 z stacks from 6 fish, Figure S1E).

To facilitate comparison of tracing results across datasets, we described the x,y-position of FuGIMA neuron somata relative to a previously defined coordinate system origin (as in Kubo et al., 2014). For this, we extracted soma coordinates from .swc files, subtracted the origin coordinates (intersection of planes connecting the anterior tips of the AF9 containing neuropil, the midline, and the plane just dorsal to the anterior tips of AF9), and transformed the coordinates (45° rotation between the RGC and FuGIMA standard brain volumes). Soma locations (relative to the origin) were plotted in histograms (bin size = 16 μm, visually determined).

To combine visualization of neuronal tracings with landmark annotations, the latter were transformed to surfaces. For this, registered z stacks were binarized, if necessary manually smoothed (both using Fiji), and surface renderings were produced using the software Amira (Thermo Fisher Scientific/FEI, smoothing: unconstrained smoothing, extent = 5). Neuronal tracings and landmark surfaces were plotted using R with the packages rgl (Adler, Murdoch, and others) and NeuroAnatomy Toolbox package (Jefferis and Manton, 2014). For the accompanying videos, FuGIMA tracings were smoothed. The video was assembled using Fiji, then converted and compressed with the software FFmpeg.

Integration of RGC and FuGIMA datasets

We had generated consensus AF masks in the RGC standard brain (see section Segmentation of AFs and 3D rendering above). To transfer these masks into the FuGIMA volume, we applied a two-step registration process (Figure S3A): 1) we registered the RGC standard brain (based on *isl2b:Gal4, UAS:mCherry*) to individual "bridge"-z stacks of fish expressing *isl2b:Gal4, UAS:GFP, HuC:lyn-tagRFP* (n = 7 z stacks from 4 fish), 2) then we registered the "bridge"-z stacks to the FuGIMA standard brain (based on *HuC:lyn-tagRFP*). As we observed slight differences in the localization of co-registered AF masks, we applied a kernel-density estimation (KDE) to the collection of binarized z stacks. After normalizing the maximum pixel intensity to 100, the stack was thresholded (pixel values = 25, 50, 75, and 90) and surfaces were generated. We utilized the KDE = 50% mask for further analysis of tracing intersections with AFs.

To compare FuGIMA tracings with functional information (z stacks), we first registered the functional imaging datasets (DS in RGC terminals and all neurons) to the FuGIMA standard brain. Streaks of DS pixels were found in the region of the eye pigment in the pan-neuronal DS stack, resulting from noise due to PMT saturation. We removed those pixels with a mask. To convert .swc files of tracings to rastered data (z stacks) we applied a custom-written Fiji macro script. Resulting pixelated tracings were smoothed in Fiji to improve the impression of continuous neurites for display.

Complementation with the single-neuron atlas

To compare FuGIMA neurons with a single-neuron atlas (Kunst et al., 2019), we registered the FuGIMA dataset to the standard brain of this single-neuron atlas. The single-neuron atlas standard brain is based on the synapsin pattern (antibody staining, fixed samples) and contains several registered expression patterns to enable registration of external datasets based on those patterns (e.g., fixed *HuC:lyn-tagRFP*). To register the FuGIMA standard brain (acquired live, a sub-volume of the fish brain) into the single-neuron atlas volume (fixed, whole-brain), we employed registration in three steps a follows: 1) FuGIMA volume to a sub-volume of the live *HuC:lyn-tagRFP* standard brain (at this time not yet registered to the single-neuron atlas), 2) extension to the full live standard brain volume, 3) live standard brain to fixed *HuC:lyn-tagRFP* standard brain. Co-registration of FuGIMA tracings (.swc files) and landmark annotations (.tiff stacks), followed by surface rendering of landmarks allowed to visualize both datasets together. We searched among 1743 tracings from the web-interface of the single neuron atlas for tracings complementing the FuGIMA tracings (Pretectal projection neurons, PPNs) (https://fishatlas.neuro.mpg.de/zebrafishatlas/, download: 25. Oct. 2018, combined results of searches in different brain regions). To define the search volume for PPNs (FuGIMA VOI), we dilated FuGIMA somata and merged patches in the binary .tiff stack (distance surface to soma approx. 10 μm (x/y) and 11 μm (z), in the FuGIMA standard volume). After co-registration of the FuGIMA VOI to the single-neuron atlas volume, we identified PPNs with somata in the FuGIMA VOI (custom written python script). For the innervation analysis, we retrieved the number of tips per PPN for all 78 brain region annotations and one additional area "contralateral hemisphere." To focus on the most prominently targeted areas, we depicted areas with > 5 intersecting PPNs, omitting similar annotations i.e., only "cerebellum," no additional "corpus cerebelli," and included all annotated AFs intersecting with PPNs. For visualization, we ordered the list starting with the contralateral hemisphere, then in the order of the number of intersections.

QUANTIFICATION AND STATISTICAL ANALYSIS

The statistical information is provided in each of the sections above.

The analyzed number of zebrafish and brains is indicated in the main text and figure legends. Error bars correspond to SEM unless stated otherwise.

DATA AND SOFTWARE AVAILABILITY

Data and software will be made available upon request.